

The AMMA Land Surface Model Intercomparison Experiment coupled to the Community Microwave Emission Model: ALMIP-MEM

P. de Rosnay¹, M. Drusch¹, A. Boone²,
G. Balsamo¹, B. Decharme², P. Harris³,
Y. Kerr⁴, T. Pellarin⁵, J. Polcher⁶,
J.-P. Wigneron⁷

Research Department

¹ECMWF, UK, ²CNRM/Météo-France, France, ³CEH, UK, ⁴CESBIO,
France, ⁵LMD/IPSL, France, ⁷INRA/EPHYSE, France

Submitted to Journal of Geophysical Research

July 2008

*This paper has not been published and should be regarded as an Internal Report from ECMWF.
Permission to quote from it should be obtained from the ECMWF.*



European Centre for Medium-Range Weather Forecasts
Europäisches Zentrum für mittelfristige Wettervorhersage
Centre européen pour les prévisions météorologiques à moyen terme

Series: ECMWF Technical Memoranda

A full list of ECMWF Publications can be found on our web site under:

<http://www.ecmwf.int/publications/>

Contact: library@ecmwf.int

©Copyright 2008

European Centre for Medium-Range Weather Forecasts
Shinfield Park, Reading, RG2 9AX, England

Literary and scientific copyrights belong to ECMWF and are reserved in all countries. This publication is not to be reprinted or translated in whole or in part without the written permission of the Director. Appropriate non-commercial use will normally be granted under the condition that reference is made to ECMWF.

The information within this publication is given in good faith and considered to be true, but ECMWF accepts no liability for error, omission and for loss or damage arising from its use.

Abstract

This paper presents the African Monsoon Multidisciplinary Analysis (AMMA) Land Surface Models Intercomparison Project (ALMIP) for Microwave Emission Models (ALMIP-MEM). ALMIP-MEM consists in an ensemble of simulations of C-band brightness temperatures over West Africa for a one-year annual cycle in 2006. Simulations have been performed for an incidence angle of 55° and results are evaluated against C-band satellite data from the Advanced Microwave Scanning Radiometer on Earth Observing System (AMSR-E). The ensemble encompasses 96 simulations, for 8 Land Surface Models (LSMs) coupled to 12 configurations of the Community Microwave Emission Model (CMEM). CMEM has a modular structure which permits combination of several parameterizations with different vegetation opacity and the soil dielectric models. ALMIP-MEM provides the first inter-comparison of state-of-the-art land surface and microwave emission models at regional scale. Quantitative estimates of the relative importance of Land Surface Modeling and radiative transfer modeling for the monitoring of low frequency passive microwave emission on land surfaces are obtained. Results show that when the best microwave modeling configuration is used, all the LSMs are able to reproduce the main temporal and spatial variability of measured brightness temperature. Statistical results show a scatter in the model performances, and different LSMs provide best correlation, best standard deviation and best root mean square errors. Averaged among the LSMs, correlation is 0.67 and averaged normalized standard deviation is 0.98, both indicating good performances of the ensemble LSMs simulation. The scatter in simulated Top Of Atmosphere (TOA) brightness temperatures due to the LSMs is lower than the scatter due the choice of the microwave emission model. It is shown that for most of the LSMs, the Kirdyashev opacity model is the most suitable to simulate TOA brightness temperature in best agreement with the AMSR-E data.

1 Introduction

Soil moisture is a crucial variable of the Earth system. It controls the partitioning of energy in latent and sensible heat fluxes that occurs at the soil-atmosphere interface and it is a major variable of the continental hydrological cycle (Dirmeyer et al. (1999); Entekhabi et al. (1999); Milly and Dunne (1994)). Soil moisture strongly influences the seasonal and inter-annual dynamics of the vegetation which is an essential component of the coupled hydrological and carbon cycles (Calvet et al. (2008); Ciais et al. (2005); Foley et al. (1996); Nepstad et al. (1994)). Soil moisture is a main variable for specifying the lower boundary condition of the atmosphere. Accurate estimation of initial state soil moisture conditions is thus important for numerical weather and climate predictions. Koster et al. (2004) showed that precipitation is largely affected by soil moisture conditions and they identified three hot spot regions where feedback mechanisms between soil moisture and precipitation are strongest, in the Great Plains of North America, the Sahel, and India. Over Sahel, Taylor et al. (2007) and Taylor (2008) pointed out that soil moisture and land surface processes highly influence the dynamics of the mesoscale convective systems.

Coordinated land surface modeling activities have improved our understanding of land surface processes. The Project for the Intercomparison of Land Surface Parameterization Schemes (PILPS, Lettenmaier (2003); Henderson-Sellers et al. (1995)) has provided local scale off-line (i.e. decoupled from an atmospheric model) intercomparisons of Land Surface Models (LSMs) for more than a decade. Within the wider context of Global Energy and Water Experiment (GEWEX), PILPS is part of the Global Land Atmosphere System Study (GLASS). GLASS facilitated the development and testing of the ALMA (Assistance for Land-surface Modeling Activities) standard input/output which is the basis for intercomparison exercises. The Rhône AGGregation intercomparison experiment focused on scaling properties at regional scale over the Rhône catchment (Boone et al. (2004)). The Global Soil Wetness Project-2 (GSWP-2) provided global estimates of soil moisture and land surface fluxes Dirmeyer et al. (2006). GSWP-2 simulations were performed globally with a $1^\circ \times 1^\circ$ grid, using the International Satellite Land Surface Climatology Project (ISLSCP) Initiative II dataset for 1986-1995 (Hall et al. (2001)). The AMMA (African Monsoon Multidisciplinary Analysis) Land Surface

Model Intercomparison Project (Boone and de Rosnay (2007b); de Rosnay et al. (2006)) is being conducted for 2002-2006, at a $0.5^\circ \times 0.5^\circ$ grid. Within the AMMA project (Redelsperger et al. (2006)), one of the key objective of ALMIP is to get a better understanding of the role of soil moisture in land surface processes in West Africa. For 2004-2006, ALMIP simulations are of particular interest since two forcing datasets are available with (i) model generated forcing data and (ii) hybridized forcing data combining satellite and modeled fields (Boone and de Rosnay (2007a)).

In this paper, the main results of ALMIP-MEM (Microwave Emission Model) project are presented. ALMIP-MEM is being conducted in the joint framework of ALMIP and the future SMOS (Soil Moisture and Ocean Salinity, Kerr et al. (2001)) validation over West Africa (de Rosnay et al. (2008, 2005)). It aims at coupling the ALMIP soil moisture and soil temperature outputs provided by an ensemble of LSMs for the year 2006, to the Community Microwave Emission Model (Drusch et al. (2008); Holmes et al. (2008)) to simulate C-band (6.9 GHz) brightness temperatures as seen by the Advanced Microwave Scanning Radiometer on Earth Observing System (AMSR-E) lowest frequency channel. AMSR-E brightness temperature data are used to provide an integrated evaluation the coupled ALMIP-MEM approach. The CMEM forward model has been developed by the European Centre for Medium-Range Weather Forecasts (ECMWF) as the future SMOS forward operator. Although developed for SMOS at L-band (1.4 GHz), it is suitable for a range of frequencies between 1 GHz and 20 GHz (Drusch et al. (2008); Holmes et al. (2008)). CMEM is a modular code that considers different dielectric layers (soil, vegetation, atmosphere) contributing to the Top Of Atmosphere (TOA) brightness temperature. These microwave emission models have been individually developed, calibrated and validated at local scale based on different field experiments for different soil and vegetation types and for different climate conditions and some of them have been used at the field spatial scale based on aircraft measurements (Wigneron et al. (2007); de Rosnay et al. (2006); Jackson et al. (1999); Wigneron et al. (1996); Schmugge (1992); Jackson and Schmugge (1991); Jackson and Neill (1990); Wang and Schmugge (1980)). Gao et al. (2004) used the L-MEB model (Pellarin et al. (2003)) to simulate a 10-year time series of synthetic L-band temperature from the GSWP-2 output of four LSMs. They used aircraft measurements acquired during the GSWP2 period to evaluate the coupled approach. All these studies contributed to improve our understanding of the microwave emission over land surfaces. They were the basis for the development of the current microwave emission models. The present work represents the first coordinated microwave emission models intercomparison experiment to our knowledge.

Using 8 LSMs, ALMIP-MEM takes advantage of the skill of the land surface modeling community in intercomparison studies and combines these with 12 microwave emission model configurations of CMEM. In total 96 ALMIP-MEM brightness temperatures simulations were performed for each ALMIP experiment and these were evaluated against AMSR-E C-band data for the year 2006 over the West African Region. In contrast to the previous studies above mentioned, the purpose of this study is not to calibrate again the microwave emission models to obtain the best fit with AMSR-E data over the particular studied region. Rather, this study aims at investigating the relative importance of Microwave Emission Models and Land Surface Models on the accuracy of simulated brightness temperatures, when compared to the AMSR-E C-band brightness temperatures.

The next section presents the data and method. This includes AMSR-E data, the Community Microwave Emission Model, the AMMA Land Surface Model Intercomparison Project, the ALMIP-MEM experiments and the method for comparing AMSR-E data and ALMIP-MEM outputs. Section 3 presents the ALMIP-MEM results and section 4 provides summary and conclusions.

2 Data and method

2.1 AMSR-E Satellite data

AMSR-E on the NASA's AQUA satellite was launched in 2002. AMSR-E instruments operate in polar sun-synchronous orbits, with equator crossings at 1:30 am (descending orbit) and 1:30 pm (ascending orbit). They measure microwave brightness temperatures at five frequencies, of which C-band and X-band channels (6.9 and 10.7 GHz) are suitable for soil moisture monitoring, with an incidence angle of 55° (Njoku et al. (2003)). At C-band brightness temperature is sensitive to the very top (~ 2 cm) soil moisture, vegetation water content and effective temperature. AMSR-E products include measured brightness temperature. They are archived and distributed routinely by NASA National Snow and Ice Data Center (NSIDC) Distributed Active Archive Center (DAAC) on a global cylindrical 25 km Equal-Area Scalable Earth Grid (EASE-Grid) cell spacing (Njoku (2004)). In this study C-band brightness temperatures of AMSR-E are used.

2.2 The Community Microwave Emission Model

The Community Microwave Emission Model (CMEM) is the observation operator developed by the ECMWF to simulate low frequency passive microwave brightness temperatures (from 1GHz to 20 GHz) of the surface (Drusch et al. (2008); Holmes et al. (2008); http://www.ecmwf.int/research/ESA_projects/SMOS/cmem/cmem_index.html). The TOA brightness temperature results from the contribution of three dielectric layers (soil, vegetation, atmosphere). It is expressed at polarization p :

$$T_{Btoa,p} = T_{Bau,p} + \exp^{-\tau_{atm,p}} \cdot T_{Btov,p} \quad (1)$$

$$T_{Btov,p} = T_{Bsoil,p} \cdot e^{-\tau_{veg,p}} + T_{Bveg,p}(1 + r_{r,p} \cdot e^{-\tau_{veg,p}}) + T_{Bad,p} \cdot r_{r,p} \cdot e^{-2 \cdot \tau_{veg,p}} \quad (2)$$

$T_{Btov,p}$ (K) is the top of vegetation brightness temperature. In this formulation vegetation is represented as a homogeneous layer with an optical depth $\tau_{veg,p}$ along the viewing path, with a brightness temperature $T_{Bveg,p}$ (K). $T_{Bau,p}$ (K) and $T_{Bad,p}$ (K) are the upward and downward atmospheric brightness temperatures; $\tau_{atm,p}$ is the atmospheric optical depth. $T_{Bsoil,p}$ (K) is the soil brightness temperatures and $r_{r,p}$ is the soil reflectivity of the rough surface. In equation 2, the soil brightness temperature is expressed according to the Rayleigh-Jeans approximation for the microwave domain as the product of the soil emissivity $e_{r,p}$ and the effective temperature:

$$T_{Bsoil,p} = T_{eff} \cdot e_{r,p} \quad (3)$$

Based on equations 1, 2, 3, CMEM includes a modular choice of the physical parameterizations for the soil, vegetation and atmosphere dielectric layers, such as those used in the L-Band Microwave Emission of the Biosphere (L-MEB, Wigneron et al. (2007)) and Land Surface Microwave Emission Model (LSMEM, Drusch et al. (2001)). For the soil, as described in Drusch et al. (2008), 3 parameterizations are considered for the dielectric constant, 4 for the effective temperature, 2 for the smooth emissivity model and 5 for the soil roughness. The vegetation optical depth can be represented by a choice of 4 different parameterizations and the atmospheric opacity by 3 parameterizations. Consequently, CMEM provides a total of 1440 different configurations. This study does not test all these possible configurations. There the soil effective temperature and the atmospheric opacity models of Choudhury et al. (1982) and Pellarin et al. (2003) are chosen. The smooth emissivity is represented with the Fresnel Law and the effects of soil roughness are parameterized using the Choudhury et al. (1979) parameterization. The sensitivity of the simulated brightness temperature is investigated for different configurations of the vegetation optical depth and the soil dielectric constant. These two components of the microwave emission model are strongly related to soil moisture and vegetation water content which are the main

Table 1: Physical parameterizations used in CMEM for ALMIP-MEM. Twelve configurations are considered for different combination of soil dielectric and vegetation optical depth models.

Vegetation optical depth	Dielectric constant		
	Dobson et al. 1985	Mironov et al. 2004	Wang and Schmugge 1980
Jackson and O'Neill 1990	1	5	9
Kirdyashev et al. 1979	2	6	10
Wegmüller et al. 1995	3	7	11
Wigneron et al. 2007	4	8	12

contributors affecting the sensitivity of the TOA brightness temperature, as shown in Jones et al. (2004). Table 1 summarizes the microwave modeling parameterizations used in this study concerning vegetation opacity and dielectric models. It indicates the 12 cross configurations of vegetation opacity and dielectric models and gives an index number for each, which will be used in the following. A short description of the soil dielectric constant and vegetation opacity models used in this study is provided hereafter. More detailed descriptions of all parameterizations used in CMEM can be found in the references listed in Table 1 and given by Drusch et al. (2008).

2.2.1 Soil dielectric models

Microwave remote sensing of soil moisture relies on the large contrast between the dielectric constant of water (~ 80) and that of dry soils (~ 4). The soil dielectric mixing model relates the soil dielectric constant to the volumetric soil moisture and soil texture, frequency of detection and surface soil temperature. Several dielectric models have been proposed in the literature. The Wang and Schmugge (1980) and the Mironov et al. (2004) models consider the effect of bound water on the dielectric constant. They are limited to rather low frequencies in the range of about 1 GHz to 10 GHz. The Dobson model is valid for a larger range of frequency (1 GHz to 18 GHz), but the dielectric constants computed from the Wang and Schmugge and the Mironov models are in better agreement with measurements for a large range of soil texture types (Cardona et al. (2005); Mironov et al. (2004)). These three models are implemented for in CMEM (Table 1).

2.2.2 Vegetation opacity models

The emission of the vegetation is described in CMEM using the so-called $\tau - \omega$ approach in which the vegetation brightness temperature is expressed as a function of the canopy temperature T_c corrected by an emissivity factor related to the extinction across the vegetation:

$$T_{Bveg,p} = T_c \cdot (1 - \omega_p) \cdot (1 - e^{-\tau_{veg,p}}) \quad (4)$$

The extinction accounts for the vegetation optical depth $\tau_{veg,p}$ and the the single scattering albedo ω_p at polarization p . Based on the $\tau - \omega$ approach several parameterizations have been proposed to compute the vegetation optical thickness. The four approaches implemented in CMEM are indicated in Table 1. For each of them, the values of the parameters are indicated in Table 2 according to Holmes et al. (2008), Wigneron et al. (2007) and Pellarin et al. (2003).

Jackson and Schmugge (1991) related the optical thickness to the vegetation water content (VWC) and an empirical parameter b relating the vegetation structure:

$$\tau_{veg,p} = b \cdot \frac{VWC}{\cos\theta} \quad (5)$$

Table 2: CMEM vegetation parameters for the four considered parameterizations.

Parameterizations	Parameter	Low vegetation types		High vegetation types (Forest)		
		Crops	Grass	Rain	Deciduous	Coniferous
Jackson, Kirdyashev, Wegmüller	ω	0.05		0.05		
	VWC	0.5.LAI		10	4	3
Kirdyashev, Wegmüller	ageo	0.33		0.66		
Jackson	b	0.2	0.15	0.33		
Wigneron	b'	0.2	0.2	0		
	b''	0	0.00	0.7	0.69	0.7
	ω	0.05		0.095	0.07	0.08
	tth	1	1	1	0.49	0.8
	ttv	1	1	1	0.46	0.8

The b parameter is determined from field experiments for different vegetation types and the VWC is expressed as a linear function of the Leaf Area Index (LAI) (Pellarin et al. (2003)). In this parameterization the single scattering albedo is constant for low and high vegetation types.

In the Wigneron et al. (2007) vegetation optical thickness model, the single scattering albedo depends on both vegetation type and polarization. The polarized optical thickness is expressed as:

$$\tau_{veg,p} = \tau_{nadir} \cdot (\cos^2 \theta + tt_p \sin^2 \theta) \frac{1}{\cos \theta} \quad (6)$$

$$\tau_{nadir} = b' \cdot LAI + b'' \quad (7)$$

where tt_p parameters represent the angular effect on vegetation optical thickness for each polarization and vegetation types. τ_{nadir} is the nadir optical depth and b' , b'' are the vegetation structure parameters. Parameters used at C-band for this study for short vegetation types (crops and grass, Table 2) are based on Wigneron et al. (1995) and Pellarin et al. (2006).

The Kirdyashev et al. (1979) parameterization is simple in terms of number of parameters, but it accounts for the observing frequency. It expresses the vegetation optical thickness as a function of the wave number k (between 1 GHz and 7.5GHz), the dielectric constant of vegetation water, ϵ''_{vw} (imaginary part), VWC, incidence angle θ , water density ρ_{water} and a vegetation structure parameter a_{geo} :

$$\tau_{veg,p} = a_{geo} \cdot k \cdot \frac{VWC}{\rho_{water}} \cdot \epsilon''_{vw} \cdot \frac{1}{\cos \theta} \quad (8)$$

This parameterization has been used by Kerr and Njoku (1990) to investigate the multi-frequency microwave signal over semi-arid regions.

It was extended to a larger range of frequencies (1-100 GHz) by Wegmüller et al. (1995), by accounting for the wave number in the attenuation along the viewing path.

2.2.3 Subgrid-scale variability

The brightness temperature at the top of the vegetation ($T_{Btov,p}$, equation 2) can be computed for each model grid box taking the sub-grid scale variability of the land surface into account. Up to seven tiles can be considered in each CMEM grid box: bare soil, low vegetation, high vegetation (each are either free of snow or snow-covered) and open water. For low and high vegetation tiles, the dominant type is determined from the land cover data base. Within each grid cell, brightness temperatures are computed separately for each tile. The grid cell averaged brightness temperature is computed using the weighted sum of each tile.

2.2.4 Forcing variable and parameters

To simulate TOA brightness temperatures CMEM requires (i) dynamic fields: the soil moisture and soil temperature profiles, 2m air temperature, LAI, snow depth and snow density, and (ii) static fields: soil texture, land cover, and geopotential at the surface which represents the surface elevation. More details concerning CMEM input/outputs are provided in [Drusch et al. \(2008\)](#). For the ALMIP-MEM simulations performed in this study, the dynamic fields are obtained from the individual ALMIP simulations for each LSM. The static fields are provided by the ECOCLIMAP data base for soil texture and land cover ([Masson et al. \(2003\)](#)) and from the ECMWF forecast for the geopotential at the surface.

2.3 AMMA Land Surface Models Intercomparison Project (ALMIP)

ALMIP is being conducted within the AMMA project ([Boone and de Rosnay \(2007a\)](#); [de Rosnay et al. \(2006\)](#); http://www.cnrm.meteo.fr/amma-moana/amma_surf/almip/index.html). It intercompares results from several LSMs in order to determine which processes are missing or not adequately modeled by the current generation of LSMs over this region.

LSMs require the following input forcing fields: precipitation, short-wave and long-wave radiative fluxes, wind speed and direction, 2m air humidity and temperature, surface pressure. For each LSM, two ALMIP experiments were conducted with different precipitation and radiative fluxes forcing. In the control experiment of ALMIP (EXP1), the LSMs have been forced with the ECMWF forecasts (FC) for 2001-2006. In the second experiment (EXP2), forcing have been obtained for 2004-2006 from ECMWF-FC fields hybridized with the satellite based precipitation products obtained in EPSAT-SG (Estimation des Pluies par SATellite - Seconde Génération, [Chopin et al. \(2004\)](#)) and the OSI-SAF (OceanS and Ice - Satellite Application Facility) and Land-SAF radiative fluxes for 2004 and 2005-2006, respectively ([Boone and de Rosnay \(2007a\)](#); [Geiger et al. \(2008\)](#)). [Boone and de Rosnay \(2007a\)](#) have shown that the hybridized forcing data set used in EXP2 is more realistic. In particular, Northward extend of the monsoon is better represented than in the ECMWF-FC precipitation which underestimates rainfall occurrence and intensity over Sahel.

2002-2003 forcing data have been used repetitively to spin-up the LSMs. For 2004-2006, both EXP1 and EXP2 were performed at a 0.5° resolution in latitude and longitude over the West African domain (from 5°S to 20°N in latitude and from 20°W to 30°E in longitude). ALMIP outputs have been provided from each LSM at a 3 hour time step. They include, among other surface fields, soil moisture and soil temperature profiles, sensible and latent heat fluxes and runoff.

In ALMIP-MEM 8 LSMs has been coupled to the CMEM forward operator (Table 3). Five of them are completely independent and three are derived versions of TESSEL and ISBA LSMs. Apart from ISBA-FR, which uses a force restore approach, all these LSMs use a physically based explicit representation of the soil hydrology by solving the Darcy equation extended to unsaturated soil. The thickness of the surface soil moisture layer is highly variable between the LSMs, ranging from millimeters (ORCHIDEE-CWRR and Noah) to 1 cm (ISBA-FR), 3 cm (ISBA-DF), 7 cm (HTESSEL, TESSEL, CTESSEL) and 10 cm (JULES). For the coupling with CMEM, the top layer soil moisture is used, except for ORCHIDEE-CWRR and Noah which consider a very fine vertical discretization. For these two LSMs, soil moisture is aggregated over the first top 4 layers and top 2 layers, respectively, leading to a thickness of 2.15 cm for ORCHIDEE-CWRR and 2 cm to 10cm for Noah which uses variable soil depths. H-TESEL (H stands for Hydrology, [Balsamo et al. \(2008\)](#)) is an improved version of TESSEL ([Viterbo and Beljaars \(1995\)](#)). It is currently used operationally at ECMWF for numerical weather prediction. It accounts for variable runoff infiltration scheme as a function of soil texture and orography. CTESSEL (Carbon TESSEL, [Jarlan et al. \(2007\)](#)) results from the coupling between TESSEL and ISBA-A-gs ([Calvet et al. \(1998\)](#)). It describes the coupling between carbon and water cycles through a

Table 3: Land Surface Models used for ALMIP-MEM.

Name	Group	Soil hydrology	Reference
ISBA-FR	CNRM/Météo-France	Force Restore	Noilhan and Planton (1989)
ISBA-DF	CNRM/Météo-France	Diffusion	Boone et al. (2000)
HTESSEL	ECMWF	Diffusion	Balsamo et al. (2008)
TESSEL	ECMWF	Diffusion	Viterbo and Beljaars (1995)
CTESSEL	ECMWF	Diffusion	Jarlan et al. (2007)
JULES	MetOffice	Diffusion	Blyth et al. (2006) Essery et al. (2003)
Noah	NCEP/EMC	Diffusion	Chen and Dudhia (2001) Decharme (2007)
ORCHIDEE-CWRR	IPSL	Diffusion	d’Orgeval (2006); de Rosnay et al. (2002) Krinner et al. (2005)

diagnostic computation of plant LAI and control of latent heat flux by the plants. ISBA-DF (diffusion scheme) is an option of ISBA (Noilhan and Planton (1989)) which accounts for multi-layered explicit soil heat and water transfer (Boone et al. (2000)). JULES is the Met Office Surface Exchange Scheme (MOSES, Essery et al. (2003)), coupled to Top-down Representation of Interactive Foliage and Flora Including Dynamics (TRIFFID). It accounts for plant transpiration, soil evaporation, plant growth and soil respiration (Blyth et al. (2006)). Noah is used in the National Center for Environmental Prediction (NCEP) global Medium-Range Forecast model (Chen and Dudhia (2001)). In this study, a recently improved version is used in which the Dunne runoff is computed via a sub-grid distribution of the topography using a new TOPMODEL approach (Decharme (2007)). ORCHIDEE is the Institut Pierre-Simon Laplace land surface model (Krinner et al. (2005)). In the CWRR version used in this study, the soil water dynamics is physically based and the latent heat flux is controlled by the soil water and plant roots profiles (d’Orgeval (2006); de Rosnay et al. (2002)). More detailed descriptions of these models can be found in the references given in Table 3.

2.4 ALMIP-MEM Experiments

ALMIP-MEM considers the coupling between the 8 LSMs of Table 3 and the 12 microwave modeling configurations of Table 1. Combining these different LSMs and microwave models, ALMIP-MEM consists in two sets of 96 simulations conducted for the ALMIP EXP1 and EXP2 respectively. Simulations are performed for the complete year 2006 in the AMSR-E configuration at 6.9 GHz (C-band) and at 55° incidence angle.

ALMIP-MEM experiments are conducted without any calibration of the coupled LSMs-microwave emission models. Rather, we perform an inter-comparison of different combinations of state-of-the-art LSMs and microwave emission models. We address the sensitivity of the TOA brightness temperatures, to the different components of the earth modeling system, including precipitation forcing, soil moisture and land surface modeling parameterizations and microwave emission parameterizations of vegetation and soil contributions.

2.5 Statistical comparison between ALMIP-MEM and AMSR-E

In this study C-band AMSR-E brightness temperature products are used to evaluate the ALMIP-MEM ensemble simulations over West Africa. To this end AMSR-E data are linearly interpolated to the ALMIP regular 0.5°

latitude-longitude grid and a temporal collocation is performed by using the time step of ALMIP-MEM outputs which is the nearest to the AMSR-E observing time. The results presented in this paper focus on horizontally polarized brightness temperature which is the most sensitive to the soil moisture and vegetation water content variability.

To quantify each model's skill to simulate the observed brightness temperatures, we have computed three non-dimensional statistics:

1. The correlation coefficient (R). It indicates whether the simulated and observed fields have similar patterns.
2. The normalized standard deviation (SDV). It gives the relative amplitude of the variations of the simulated field compared to those of the observed field.
3. The centered Root Mean Square Error between simulated and observed patterns, (E) which is normalized by the observed field standard deviation. It relates errors in the pattern of variations. Note that centered RMSE does not include any information on the overall biases since means of the fields are subtracted before computing second order errors.

As shown in Taylor (2001), these three different statistics are complementary but not independent. They are related by:

$$E^2 = SDV^2 + 1 - 2 \cdot SDV \cdot R \quad (9)$$

Based on this relation, Taylor diagrams are generally used to represent on two-dimensional plots these three different statistics (Taylor (2001)). They display the normalized standard deviation (SDV) as a radial distance and the correlation with observations as an angle in the polar plot. Observed data are represented by a point located on the x-axis at $R=1$ and $SDV=1$. The centered normalized RMS difference (E) between the simulated and observed patterns, is the distance to this point.

Statistics are computed on a West African sub-window which the area is delimited by 9°N - 20°N and 10°W - 10°E . This window includes the North-South climatic gradient which characterizes the Sahelian area, but it eliminates the coastal grid points and the southern area where C-band signal is expected to be constantly saturated by the tropical forest vegetation water content.

3 Results

3.1 Influence of the precipitation forcing

Figure 1 illustrates an example of observed (AMSR-E) and simulated (ALMIP-MEM for ORCHIDEE in this example) brightness temperature (TB) at horizontal polarization on Days of Year (DoY) 200-201 and 220-221, for the descending orbit and in the CMEM configuration for which the dielectric constant is simulated with the Mironov model and the optical thickness with the Kirdyashev model (Table 1, configuration 6). High values of soil moisture are characterized by low emission and thus low values of TB. In contrast, areas with high vegetation water content, as encountered at latitude between 4°S and 10°N , have high brightness temperature values. Figure 1a clearly shows the presence of wet soil centered on 2°W , 15°N in the Sahelian region on DoY 200-201, with low values of TB. This typically corresponds to the occurrence of a monsoon season mesoscale convective rainfall event (Janicot et al. (2007)). This wet patch is very well reproduced by the ALMIP-MEM EXP2 simulation (Figure 1a, middle), with a spatial correlation $R=0.66$. However it is not so well simulated in EXP1 (Figure 1a, right) with $R=0.39$, for which the precipitation forcing is not corrected by satellite data. On

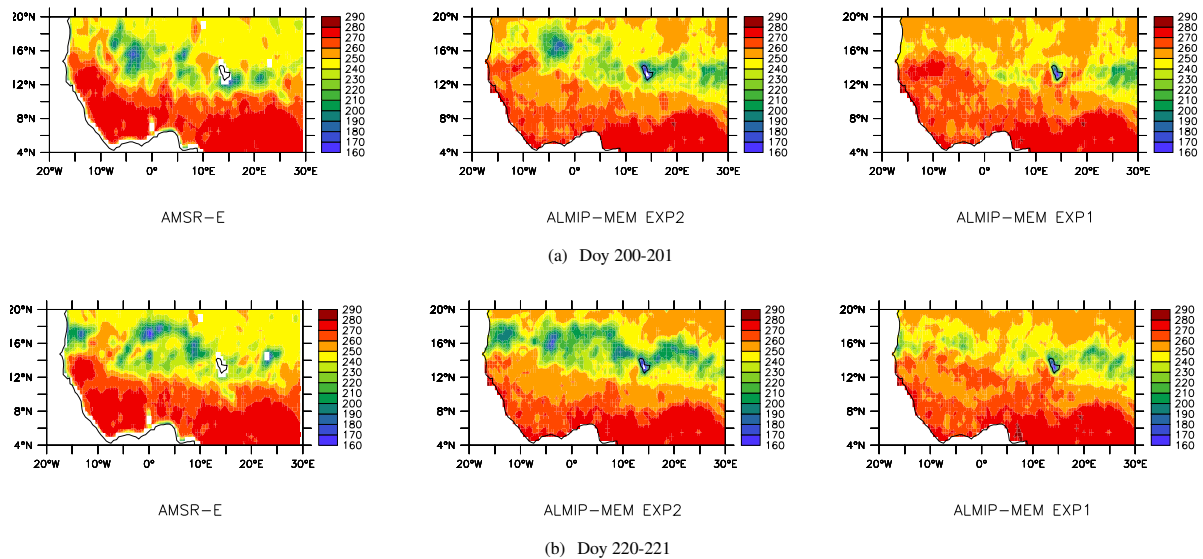


Figure 1: C-band brightness temperature (K) at horizontal polarization observed by AMSR-E (left), simulated by ALMIP-MEM for EXP2 (middle) and EXP1 (right), for DoY 200-201 (a) and 220-221. This example shows ORCHIDEE-CWRR results coupled to the Mironov dielectric model and the Kirdyashev opacity model (CMEM configuration 6 of Table 1).

DoY 220-221 (Figure 1b) the pattern is different indicating wet soil patches pattern has been evolving in space and time according to rainfall occurrence. The extend of the wet patches are slightly overestimated in EXP2 while they are underestimated in EXP1. Model performances are better than on DoY 200-201, and correlation values still indicate EXP2 to be more suitable ($R=0.71$) than EXP1 ($R=0.63$). This result is extended to the whole annual cycle and for the 8 ALMIP-MEM LSMs in Table 4 which shows statistics of the comparison between simulations and AMSR-E data for EXP1 and EXP2 when the microwave modeling configuration uses the Wang and Schmugge and Kirdyashev models (Table 1, configuration 10). This configuration is chosen to describe the differences between the LSMs and the ALMIP experiments since it is the one which provides the overall best performances in the microwave modeling approach for most of the LSMs as shown later in this paper. Land Surface Models that best represent the observations have highest correlation (R), lowest normalized root mean square error (E) and SDV value closest to one. For all the LSMs, correlation values and root mean square errors show that EXP2 (averaged values are $R=0.67$ and $E=0.83$) is in much better agreement than EXP1 (averaged values: $R=0.54$, $E=0.91$) with the observations. Six LSMs show SDV values lower than 1, which indicate an underestimation of the amplitude of the variations compared to the observations. For these LSMs, agreement with observations is also improved in terms of amplitude of variations in EXP2 with higher SDV values compared to EXP1. Two LSMs (TESSEL and CTESSEL) present standard deviation values higher than one, which indicate an overestimation of the signal amplitude. This overestimation is exacerbated in EXP2 for these two models. None of the LSMs show SDV in a 10% agreement with the observation (in the range of $[0.9;1.1]$) for EXP1. For EXP2 three LSMs are in this range (HTESSEL, Noah, ORCHIDEE-CWRR). The overall better agreement between simulations and observations in EXP2 compared to EXP1, indicates that the corrected precipitation forcing leads to better represent TB in term of variability, as well as in term of amplitude and pattern of variations.

These results emphasize the importance of the LSM's precipitation forcing for the forward modeling of brightness temperatures. They show that background errors in simulated brightness temperatures will be highly dependent on forecast errors in precipitation. In turn, this points out the high potential of assimilation of low frequency passive microwave data to correct errors in soil moisture and fluxes, related to rainfall occurrence.

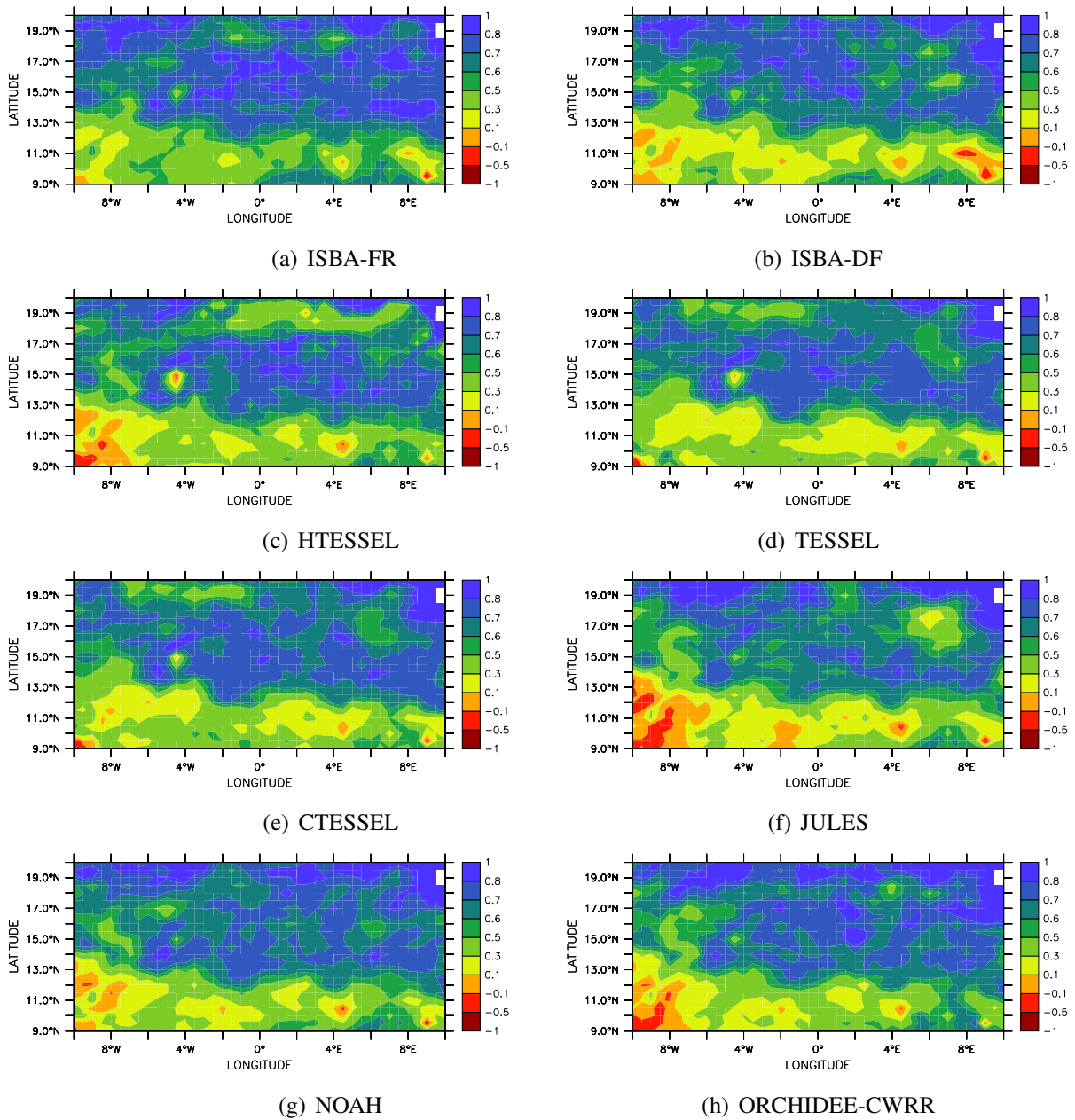


Figure 2: Map of the temporal correlation between observed and simulated C-band horizontal brightness temperature for the 8 ALMIP-MEM LSMs (EXP2) coupled to the Wang and Schmugge dielectric model and the Kirdyashev opacity model (CMEM configuration 6 of Table 1).

Table 4: Statistics of the comparison between ALMIP-MEM simulated and AMSR-E observed C-band brightness temperatures at horizontal polarization for 2006, for EXP1 and EXP2 (descending orbit). These results are for the CMEM configuration 10 (Table 1). Best agreement between modeled and observed AMSR-E brightness temperatures are obtained for $R=1$, $SDV=1$ and $E=0$ (section 2.5). Spatio-temporal correlation values are provided (left) as well as temporal correlation values as shown Figure 2 spatially averaged on the studied window (right).

LSM	Spatio-temporal						Temporal	
	EXP1			EXP2			EXP1	EXP2
	R	E	SDV	R	E	SDV	R	R
ISBA-FR	0.56	0.83	0.65	0.69	0.74	0.86	0.39	0.63
ISBA-DF	0.57	0.82	0.65	0.73	0.68	0.71	0.18	0.56
HTESSEL	0.37	1.02	0.79	0.54	0.96	1.01	0.27	0.55
TESSEL	0.50	1.11	1.18	0.67	1.02	1.36	0.24	0.56
CTESSEL	0.52	1.07	1.15	0.69	0.98	1.36	0.27	0.57
JULES	0.51	0.87	0.57	0.63	0.78	0.67	0.18	0.52
Noah	0.66	0.75	0.64	0.72	0.72	0.90	0.37	0.58
ORCHIDEE	0.63	0.78	0.71	0.71	0.75	0.94	0.34	0.58
AVERAGE	0.54	0.91	0.79	0.67	0.83	0.98	0.28	0.57

3.2 Temporal evolution of the microwave emission

Figure 2 shows the maps of the temporal correlation over the year 2006 between the AMSR-E data and the simulated TB at horizontal polarization, for the 8 ALMIP-MEM LSMs for the studied window (9°N - 20°N and 10°W - 10°E). For all the LSMs, simulated TB show contrasting results between the North of the window (Sahelian area) where correlation values indicate a good agreement with the observations, and the South of the window (Soudanian area) where correlation values are lower. Northern area (Sahel) is characterized by a very contrasted annual cycle with a short monsoon season. For the very North, only a few precipitation events occur in the year. The resulting contrasted annual cycle is well reproduced by the models, leading to high values of correlation of simulated TB with AMSR-E data. In contrast the very south of the window has a less contrasted annual cycle of TB, due to the constant presence of high vegetation types permitted by more important rainfall all along the year. This explains the low correlation values at South between simulated and observed TB. The corresponding spatially averaged values of the temporal correlation are given for the 8 LSMs in Table 4 for EXP1 and EXP2. For most of the LSMs, results show poorer performances for averaged temporal correlations than for spatio-temporal correlations. This indicates that for these models, the spatial pattern is generally better reproduced than the temporal dynamics. This is not the case for HTESSEL which shows consistent agreement with the AMSR-E observations when spatio-temporal and temporal dimensions are considered. It is interesting to notice that ISBA-FR, which is the model with the simplest parameterization of the soil hydrology, shows the best averaged temporal correlation between simulated and observed horizontal TB, with a value of 0.63.

The contrast between EXP1 and EXP2 is larger for temporal correlations than for spatio-temporal correlations. Temporal correlation of simulated TB with AMSR-E data in EXP1 are lower than 0.4 for all the LSMs. This point out that improvements in precipitation forcing between EXP1 and EXP2 not only concerns spatial scale but also improves precipitation occurrence (temporal scales) which influences the soil moisture and soil temperature dynamics. The following of this paper focuses on EXP2 results.

To investigate further the latitudinal contrast in model performances shown in Figure 2, Figure 3 plots the mean temporal evolution of observed and simulated horizontal TB for two sub-windows between 15°N and 20° (North) and between 9° and 15°N (South). For each model, brightness temperature is plotted after its mean annual bias, computed at the regional scale is removed. This allows us to focus on the simulated signal variabil-

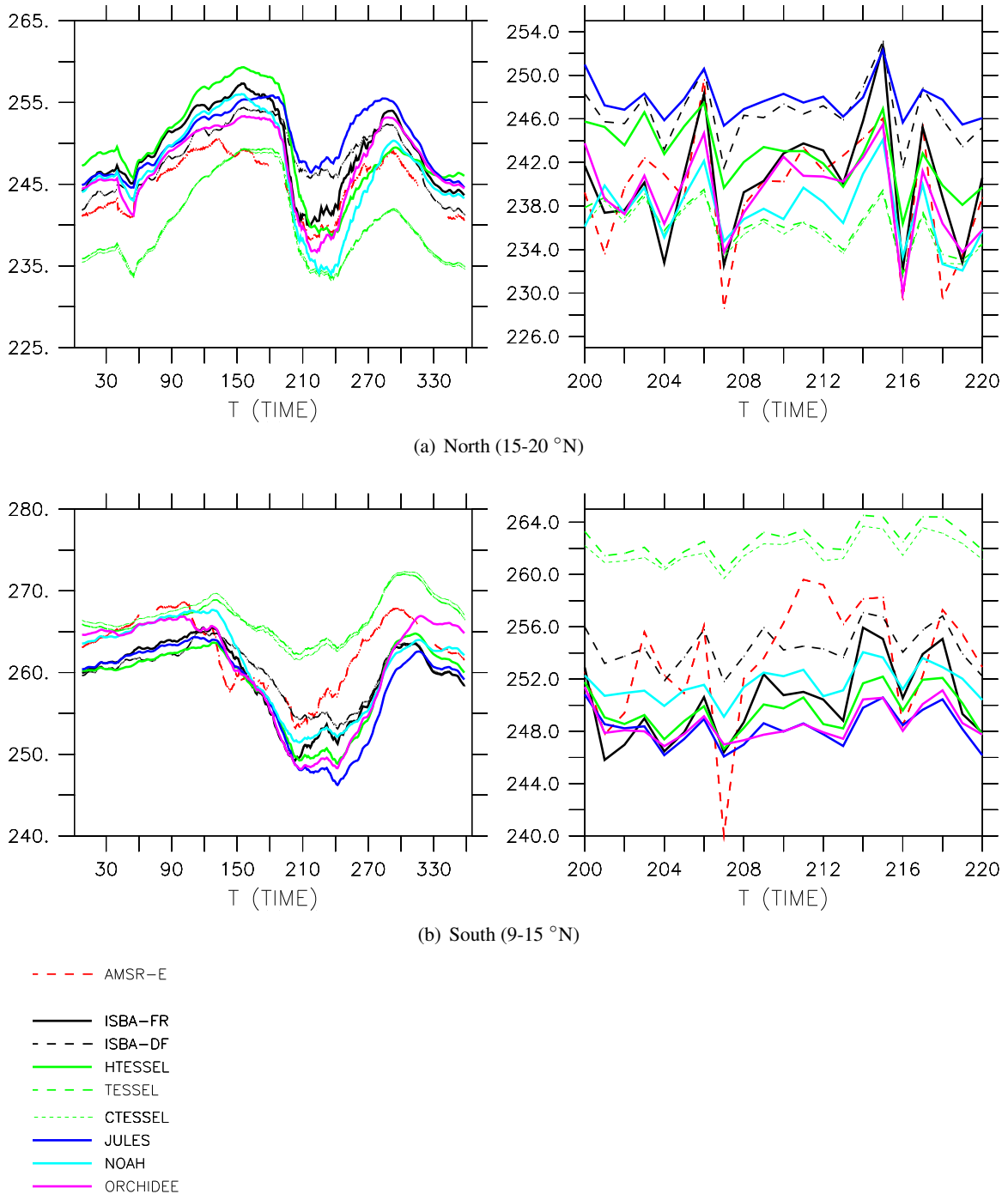


Figure 3: Temporal evolution (time in DoY) of simulated and observed horizontally polarized brightness temperature (K) from the 8 ALMIP-MEM LSMs (EXP2) coupled to the Wang and Schmugge dielectric model and the Kirдыashev opacity model (CMEM configuration 10 of Table 1). Brightness temperatures are spatially averaged for the North (a) and the South (b) of the studied window (9°North-20°North and 10°West-10°Est). The left plots shows the annual cycle with a running average of 15 days. On the right variability on shorter temporal scale is depicted between DoY 200 and 220. For each LSMs, a bias correction was applied based on the annual mean averaged bias computed on the 9°N-20°N and 10°W-10°E studied window.

ity ; and this is suitable for future assimilation of brightness temperature for Numerical Weather Prediction for which a bias correction will be applied. The annual cycles (Figure 3, left) are well reproduced by the simulations for all models. Over Sahel (North), vegetation density and vegetation water content are rather limited. The surface emission is mainly controlled by soil moisture and soil temperatures annual cycles. Maximum values of TB are reached before the monsoon season starts, around DoY 120-150 (May), which is the period of the year with highest soil temperatures and lowest soil moisture values. During the monsoon season, seasonal brightness temperature dynamics is controlled by both soil moisture and temperature with low effect of vegetation. At this stage of the year availability of soil moisture leads to high values of latent heat fluxes which decrease de surface temperature. Accordingly, the seasonal soil moisture increase and the seasonal soil temperature decrease lead to decrease TB values. At the end of the monsoon season, between DoY 240 and 280 (September-October) the occurrence of rainfall events decreases and lower values of soil moisture are associated to lower latent heat fluxes and higher temperatures, both leading to increase TB values. Between DoY 300-365 and 1-150, the soil is very dry with low dynamics and brightness temperature dynamics is controlled by the soil temperature. It reaches a minimum in December-January when the winter of the northern Hemisphere is associated to lower values of short-wave radiations. Over the southern window (Figure 3b, left), between 9° and 15° N, the monsoon onset occurs earlier in the year and the seasonal decrease of TB related to the monsoon start around the DoY 120 (end of April). Vegetation cover is more important than in the Northern window and its impact on surface emission is larger. In particular persistent vegetation cover all the year along leads to have a lower amplitude of the signal during the dry season. The 8 LSMs coupled to CMEM (configuration 10 of Table 1) reproduce particularly well the annual cycle of the signal on both the North and southern windows. This provides an indirect validation of the LSMs and the meteorological forcing at this temporal scale. This also validates the microwave emission modeling approach (CMEM in configuration 10) which allows representation of the correct seasonal amplitude of the C-band signal in contrasting soil, vegetation, atmosphere conditions.

At shorter temporal scale at which precipitation events occur, the agreement between the model and AMSR-E data is still very good in terms of correlation, for the Sahelian area (Figure 3a, right). AMSR-E data show four minima of TB on DoY 201, 207, 216 and 218. All of them are associated with a decrease in simulated TB and the amplitudes are rather well captured for ISBA-FR, HTESEL and ORCHIDEE-CWRR. But on the southern window, where vegetation layer is more important, model performances at the precipitation event scale are clearly degraded as pointed out in Figure 2.

Figure 4 shows the temporal evolution for a few days in August 2006 of simulated horizontal brightness temperature, soil temperature and soil moisture for the ALMIP-MEM grid point corresponding to the Agoufou super site located in Mali at 15.3° N, 1.5° W. This site has been instrumented in the framework of the AMMA Enhanced Observing Period (EOP, Lebel et al. (2006)). It includes a soil moisture measurement network that will be used for the future validation of SMOS (de Rosnay et al. (2008)). The soil moisture scaling properties have been investigated in de Rosnay et al. (2008) from which up-scaling a relationship is used in this figure to derive kilometric scale soil moisture from the most representative station of the network. The Agoufou soil moisture data set has also been used to evaluate AMSR-E soil moisture products by Gruhier et al. (2008).

The occurrence of a major rainfall event on DoY 231 leads to a drastic increase of observed soil moisture from very dry conditions on DoY 230 to wet conditions on DoY 231, followed by a rapid decrease on DoY 232 due to the high infiltration rate on the sandy soil of the area. The soil moisture dynamics is very well captured by most of the LSMs, which also validates the EXP2 precipitation forcing in terms of date of occurrence and intensity. There is however a large scatter in simulated soil moisture values between the LSMs. JULES, ISBA-DF tend to underestimate soil moisture values while TESSEL, CTESEL, ORCHIDEE-CWRR overestimate soil moisture values. ISBA-FR and HTESEL perform well on this site, and Noah underestimates the dynamics with overestimation of soil moisture in dry conditions and underestimation in wet conditions. The scatter in soil temperature conditions is much lower than that of brightness temperatures. Observed AMSR-E horizontal

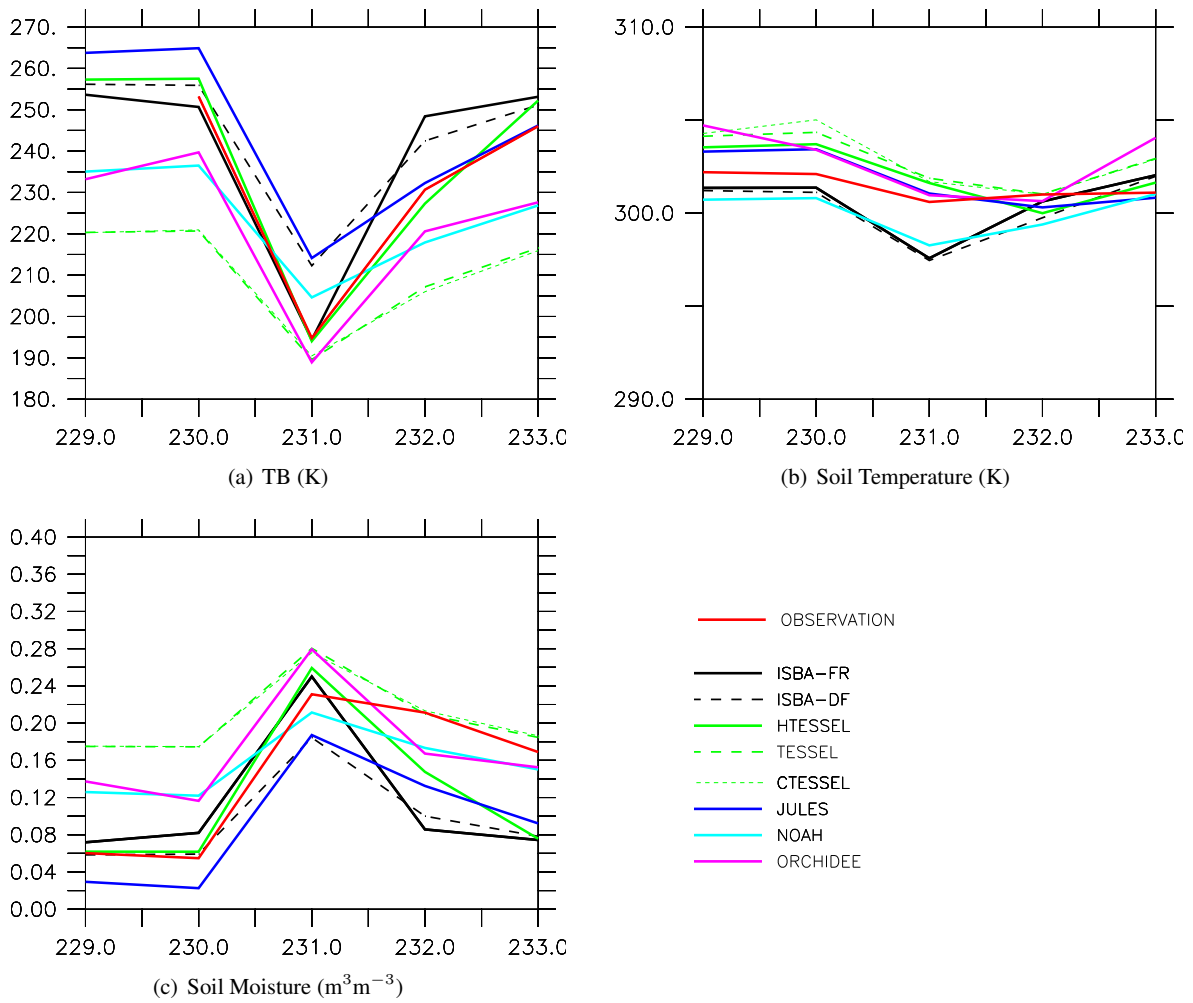


Figure 4: Temporal dynamics of simulated and observed the horizontal brightness temperature (a), soil temperature (b), and surface soil moisture (c), between DoY 229 and 233 (17-21 August). Brightness temperature observations are AMSR-E C-band data. Soil moisture and soil temperatures observations are field measurements obtained on the Agoufou super site at 15.3°N, 1.5°W (de Rosnay et al. (2008)). Simulated TB are obtained with the configuration 10 of Table 1.

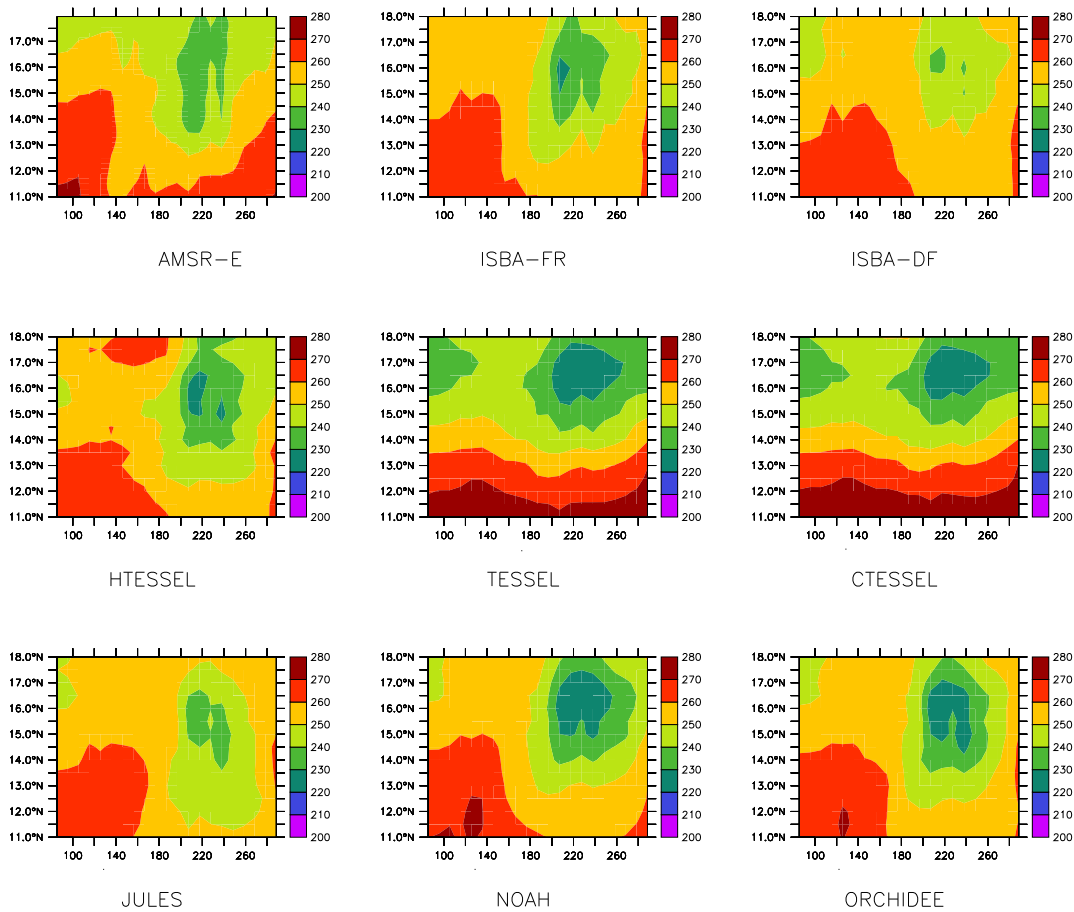


Figure 5: Time-latitude diagram of the horizontally polarized brightness temperature (K) observed by AMSR-E and simulated by ALMIP-MEM for EXP2 (CMEM configuration 10 of Table 1). For each ALMIP-MEM simulation a bias correction was applied, specifically computed for each LSM when comparing simulated and observed brightness temperature.

TB show a 55K decrease between DoY 203 and 231. The decrease is very well simulated by most of the LSMs. For each LSM, errors in simulated soil moisture are translated into errors in simulated TB. On DoY 231, in wet conditions, models which underestimate surface soil moisture (ISBA-DF, JULES, Noah) overestimate TB values. ISBA-FR and HTESSEL simulate soil moisture values in agreement with field observations and provide horizontal TB in good agreement with AMSR-E data. In contrast, LSMs that overestimate soil moisture underestimate TB. Although limited to one pixel it is interesting to compare our simulations with independent space and ground based observations. This triangular comparison between our simulations of soil moisture and TB with field and AMSR-E data provides a validation for this case study of the precipitation forcing, the LSMs and the microwave emission model on this pixel.

3.3 Time latitude distribution

Figure 5 represents the time-latitude diagram of the 10-day averaged horizontal brightness temperature at C-band for AMSR-E and simulated within EXP2 by the eight LSMs indicated in Table 3. As for the Figures 2 and 3, the simulated TB are obtained from each LSM coupled with CMEM using Kirdyashev vegetation opacity model and Wang and Schmugge dielectric model. AMSR-E C-band data show a wet patch over Sahel during the rainy season, centered at Day of year 210 and latitude 15.5° North. This wet patch is reproduced by all

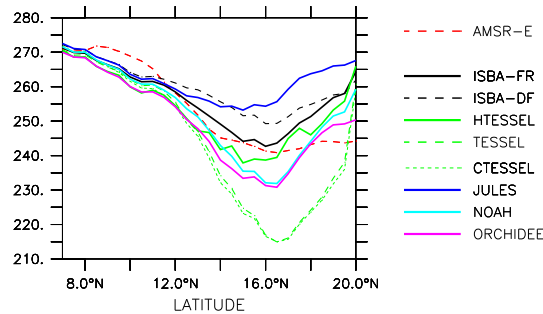


Figure 6: Zonal distribution of observed and simulated brightness temperatures (K) at horizontal polarization, averaged over July August September, for the 8 ALMIP-MEM LSMs (EXP2) coupled to CMEM using Wang and Schmugge and Kirdyashev models (CMEM configuration 10 of Table 1).

the LSMs, but the amplitude is either overestimated or underestimated depending on the LSM. In agreement with Figure 3 (left), this figure underlines the general good agreement between the forward approach and the satellite data at the annual cycle scale.

3.4 Relative role of LSMs and microwave emission models

Figure 6 shows the latitudinal plot of simulated and observed horizontal brightness temperatures averaged for the monsoon season July-August-September (JAS). It considers the simulations performed in the configuration 10 of CMEM (Table 1), but in contrast to the Figures 3 and 5 no bias correction has been applied to this plot.

From 7°N to about 12°N, there is a general good agreement between the simulated and observed TB. The scatter between the LSMs is very low, which indicates that the different soil moisture and soil temperature patterns simulated by the LSMs do not affect much the signal. Rather, this indicates that the vegetation contribution has a dominant role on the simulated and observed TB.

From 12°N to 16°N the latitudinal gradient is characterized by a decrease in both vegetation cover and soil moisture which have opposite effects on the simulated TB. The observed decrease in TB indicates that the vegetation contribution still dominates the signal. The simulations reproduce this latitudinal decrease in TB, although it is overestimated by some of the models. The scatter between the models is increasing with latitude, as the relative contribution of soil emission become more important. It reaches a maximum amplitude (40K) at 16°N. The strong negative bias of TESSEL and CTESSEL over Sahel is due to an overestimation of soil moisture by these models. Accounting for variable infiltration and soil texture in HTESSEL leads to simulation of TB in a better agreement with the observations.

From 16°N to 20°N, simulated TB increases for all the LSMs. For all of them this corresponds to a latitudinal decrease in soil water content. In contrast, AMSR-E observations do not show any latitudinal gradient in this range of latitude, indicating the end of the transition zone to the desert area.

Figure 7 shows the latitudinal distribution of simulated and observed horizontal TB for the 8 LSMs and for the 12 CMEM configurations. For each LSM, the scatter due to microwave emission model configuration is as important as the scatter shown in Figure 6 for one microwave model and several LSMs. It reaches about 40K at 10°N for most of the LSMs. In contrast to that obtained for different LSMs, the scatter due to the

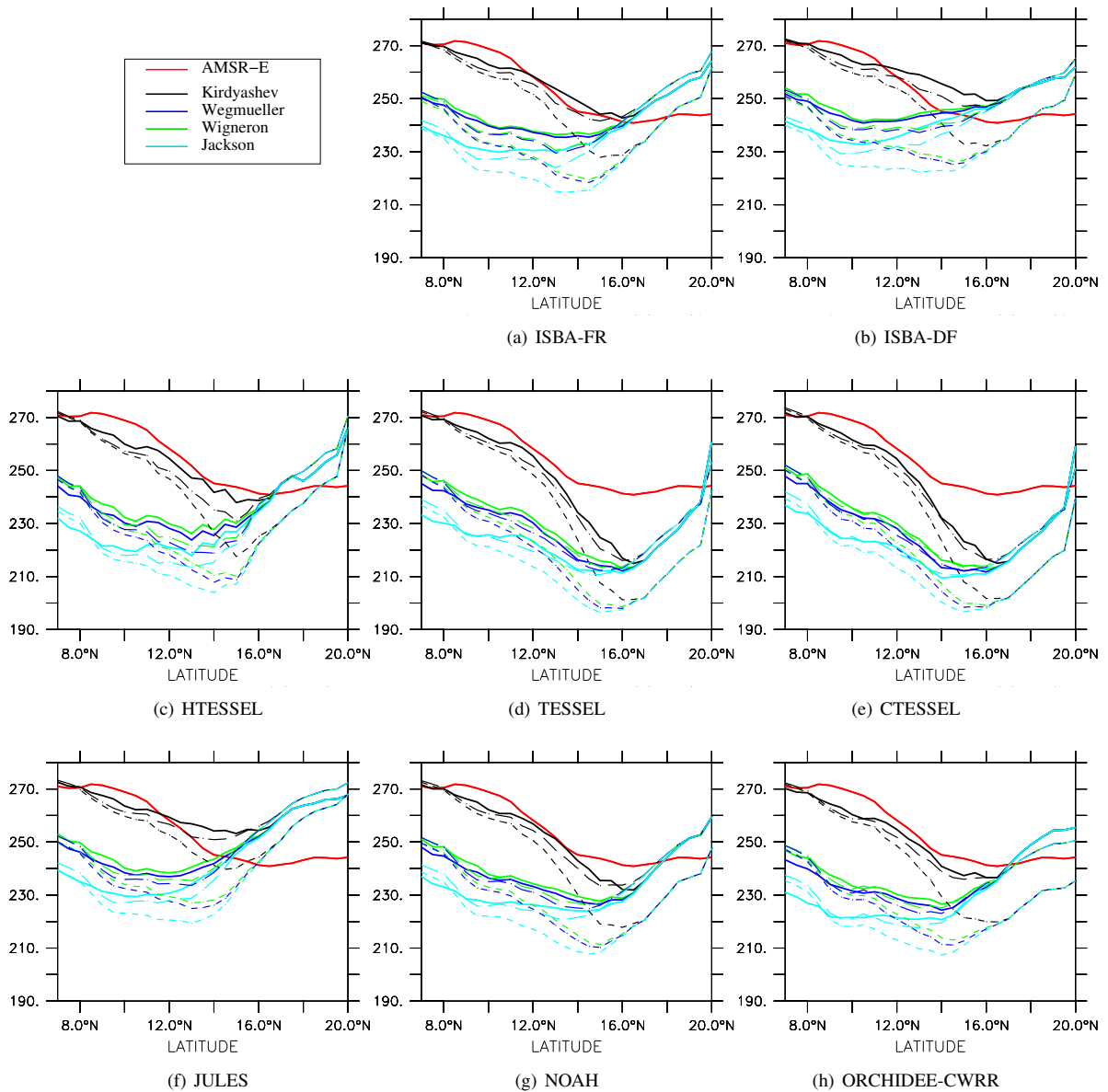


Figure 7: Zonal distribution of observed and simulated brightness temperatures (K) at horizontal polarization, for the 8 ALMIP-MEM LSMs (EXP2). For each LSM, brightness temperatures have been simulated for the 12 configurations of CMEM given in Table 1. Line color indicates the vegetation model and line style indicates the dielectric model: full line for Wang and Schmugge, dashed line for Mironov and dotted line for Dobson.

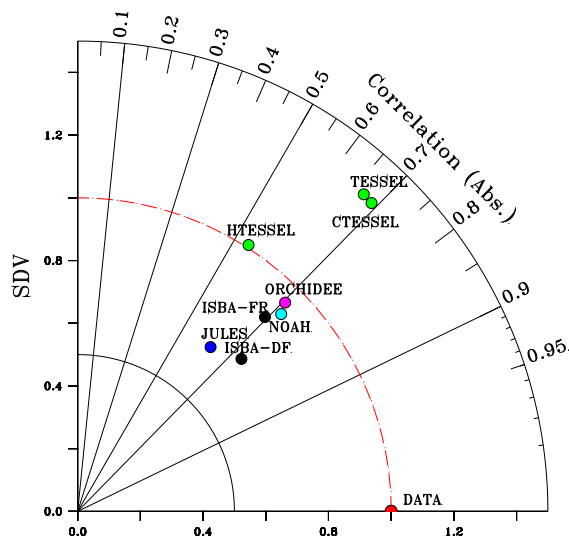


Figure 8: Taylor diagram illustrating the statistics of the comparison between ALMIP-MEM EXP2 synthetic horizontal brightness temperature and AMSR-E data at C-band for different LSMs coupled to CMEM using the Wang and Schmugge dielectric model coupled to the Kirdyashev vegetation opacity model (CMEM configuration 10, Table 1). Each circle indicates for the considered LSM, the correlation value (angle), the normalized SDV (radial distance to the origin point) and the normalized centered root mean square error (distance to the point marked “Data”).

microwave emission model is more important for southern latitudes where it is related to the vegetation opacity model. From 12°N vegetation cover decreases, and the scatter due to the opacity model decreases until the latitude 16°N is reached. Despite of the large scatter shown between the microwave emission models, it is interesting to notice that the results obtained by the Wigneron’s opacity model are very close to those obtained with the Wegmuüller model. For any LSM considered in this study, the Kirdyashev opacity model (black lines) is shown in Figure 7 to be the closest to the AMSR-E observations for the JAS average. This result must be taken with care because it might be sensitive to uncertainties related to the vegetation data base which is used (ECOCLIMAP). However the robustness of the good performances of the Kirdyashev among the different LSMs is noteworthy. North to 16°N there is no more vegetation in the ALMIP simulations and the scatter in simulated TB is due to the dielectric model only. Therefore the 12 microwave models converge to 3 microwave models which differ in their parameterization of the soil dielectric constant.

Along the North-South gradient, the scatter due to the soil dielectric model is lower than that resulting from vegetation opacity. It is increasing with the latitudinal decrease of vegetation density. For any LSM and any latitude the Wang and Schmugge model (full line) leads to higher brightness temperatures than the Dobson model (dotted line). The Mironov model (dashed line) provides intermediate values close to those of the Wang and Schmugge model.

A condensed quantitative view of the EXP2 results for the horizontal brightness temperature is provided by Figure 8, for CMEM configuration 10 (Table 1). This Taylor diagram quantifies the relative skill with which the different LSMs participating in ALMIP-MEM simulate the spatial and temporal patterns of C-band brightness temperatures. Best simulations are the nearest to the point “Data,” indicating they have highest correlation and lowest root mean square errors difference with observations. Models lying on the dashed red arc have the correct standard deviation, which indicates that the amplitude of simulated variations are in agreement with that of observations.

Each LSM uses the same atmospheric forcing and the same microwave emission model. The scatter of the per-

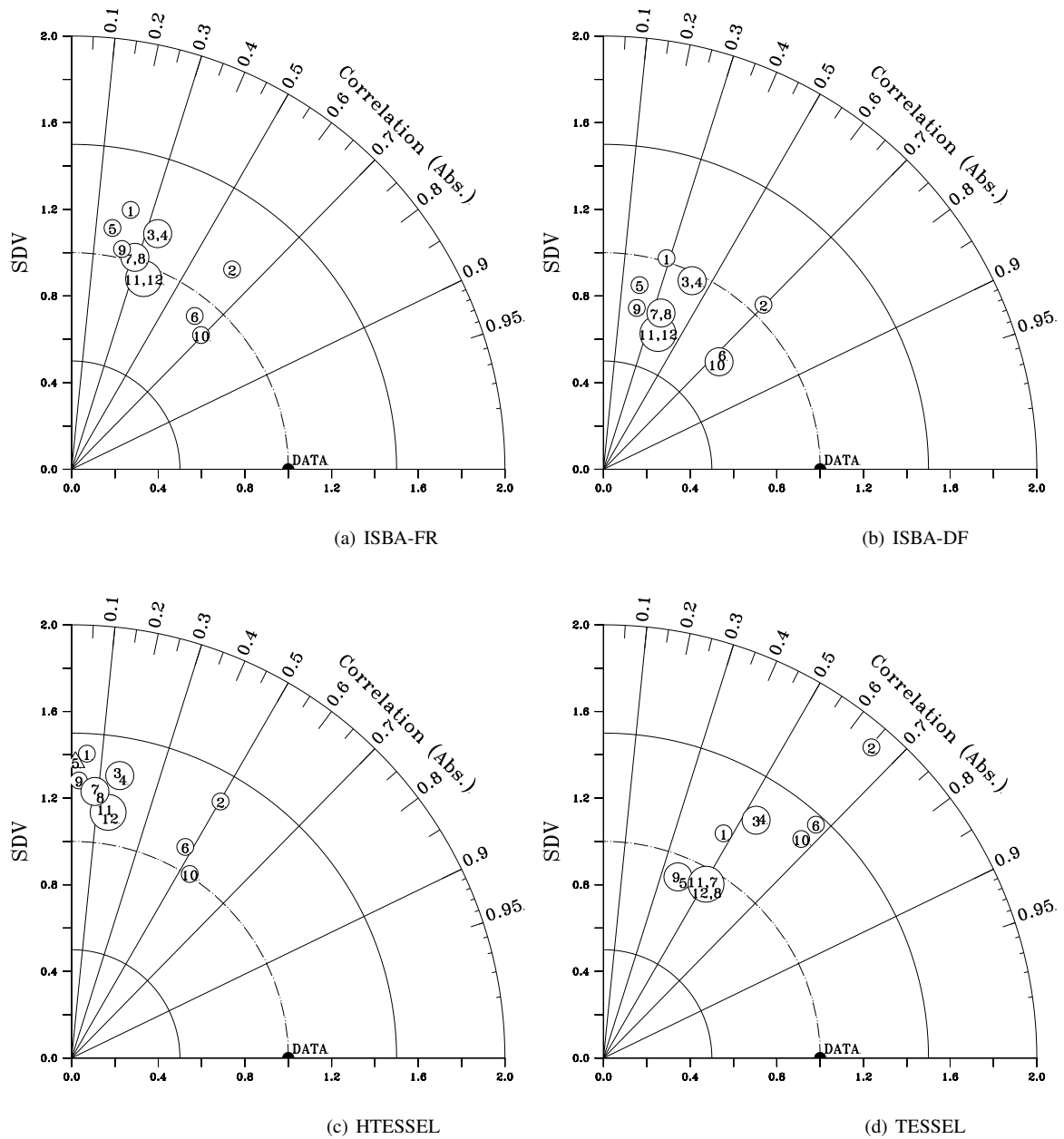


Figure 9: Taylor diagram illustrating the statistics of the comparison between ALMIP-MEM EXP2 synthetic brightness temperature and AMSR-E data at C-band for ISBA-FR (a), ISBA-DF (b), HTESSEL(c) and TESSEL(d) coupled to CMEM using the 12 different configurations of the microwave emission modeling defined in Table 1. Note that the radial axis is different from that of Figure 8. Triangular symbol indicate negative value of correlation, while circles correspond to positive values. The number within each circle indicates to which model of Table 1 these statistics refer.

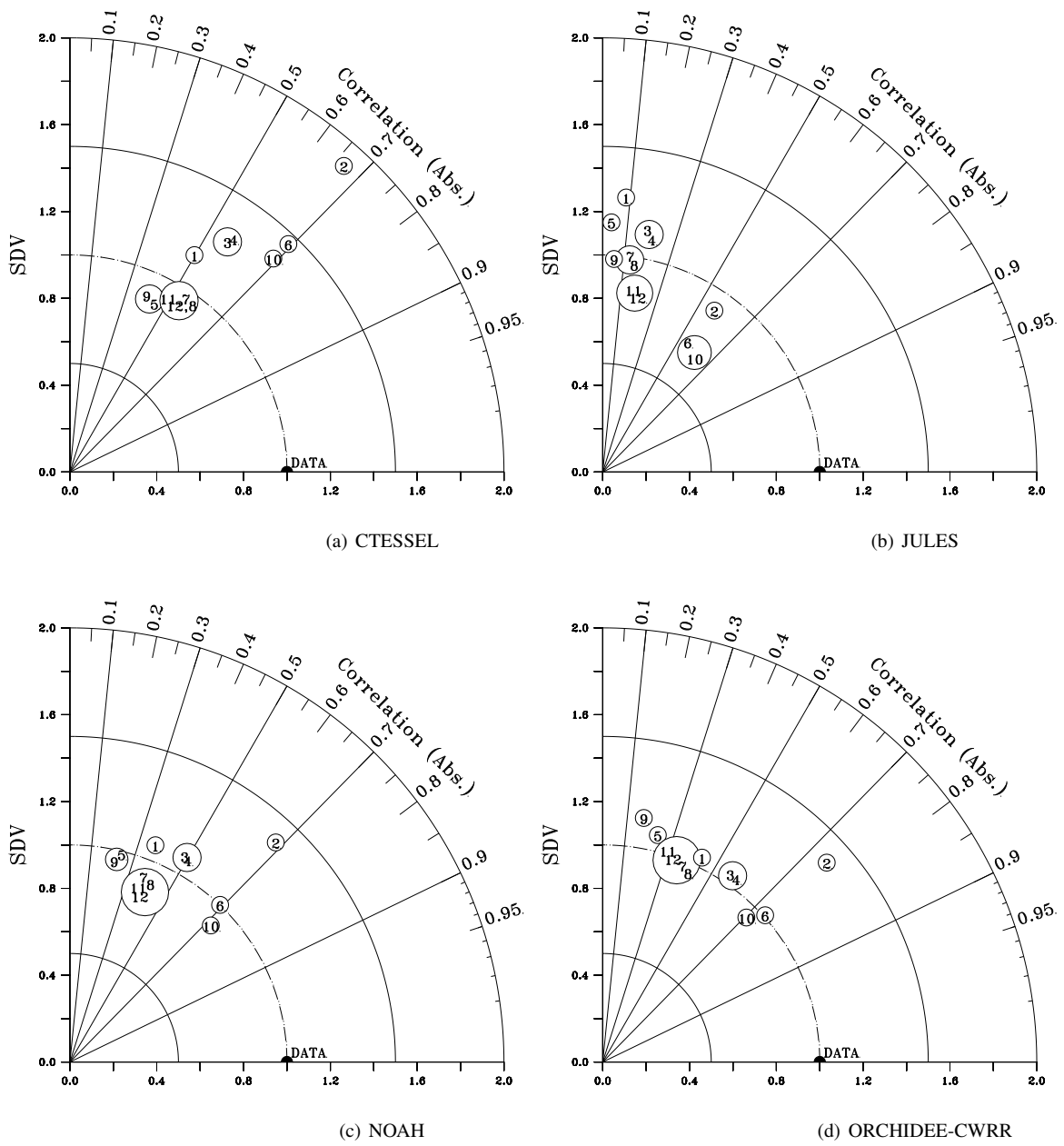


Figure 10: Same as Figure 9, but for CTESSEL (a), JULES (b), Noah (c) and ORCHIDEE-CWRR (d).

performances obtained for the different LSMs results from differences in land surface processes parameterizations which lead to different simulations of soil moisture and soil temperature profiles. In agreement with statistics provided in Table 4, Figure 8 shows that the relative SDV is in the range of 0.67 to 1.36 and correlation values between modeled and observed brightness temperatures vary between 0.54 and 0.73 depending of the considered LSM. HTESSEL SDV is very close to one. It captures very well the amplitude of the spatio-temporal variations of C-band brightness temperatures over West Africa for 2006. ISBA-DF has a low value of relative SDV, which indicates that it underestimates the amplitude of the variations. But it shows very good correlation and lowest RMS difference with the observations. When statistics are considered individually, model performances seems not related to the LSMs soil layer thickness. For example TESSEL and JULES both consider a relatively thick top soil layer (7cm and 10cm), but their performance to reproduce the observed SDV are drastically different (overestimates and underestimates respectively). Some LSM perform well in terms of correlation with poor agreement with data in terms of SDV (ISBA-DF), other do a good job to reproduce SDV with poor correlation (HTESSEL). However, it is clear from this Taylor diagram that the three LSMs that account for finest vertical discretizations in the soil (ORCHIDEE-CWRR, Noah and ISBA-FR) provide overall best results when the three statistics are considered. This result is an indication that fine soil discretization is required to simulate C-band microwave emission in good agreement with satellite data.

Figures 9 and 10 are the Taylor diagrams obtained for EXP2 simulated brightness temperatures (horizontal polarization), for each of the 8 LSMs for the 12 microwave modeling configurations. Compared to Figure 8, Figures 9 and 10 shows that the scatter due to the microwave emission model is larger than that due to the LSMs.

For example ISBA-FR results indicate that the scatter in model performances vary from 0.86 (CMEM configuration 10) to 1.23 (CMEM 1) in term of SDV, from 0.17 (CMEM 5) to 0.69 (CMEM 10) for the correlation and from 0.74 (CMEM 10) to 1.37 (CMEM 5) for E. ISBA-DF simulations lead to a lower scatter than ISBA-FR in terms of E (0.68 for CMEM 5 to 1.19 for CMEM 10). One LSM-microwave configuration results in negative correlation with the observations (triangle symbol) for HTESSEL with the Jackson opacity model and the Mironov dielectric model. TESSEL and CTESSEL simulations are characterized by a large scatter in term of SDV. This indicates a strong sensitivity of the simulated amplitude of the brightness temperature variations to the microwave emission model and to the combination between LSM and microwave model. ISBA-DF, Noah, ORCHIDEE-CWRR have correlation values higher than 0.7 when CMEM is used in configurations 10 and 6 (and also in configuration 2 for ORCHIDEE-CWRR).

For each LSM, the range of correlation values between simulated and observed TB is very large, indicating that the spatio-temporal correlation between simulated and observed TB is very sensitive to the choice of the microwave emission model. Although different sensitivities to the microwave emission model are obtained depending on the considered LSM, the scatter in correlation due to the soil dielectric model is generally less important than that due to vegetation opacity. In contrast, the scatter in SDV is more related to the soil dielectric model than to the vegetation opacity model. For each LSM, the best microwave modeling configuration is indicated in Table 5 with regard to the three statistical indexes used in this study (R, E, SDV). Except for TESSEL and CTESSEL, the best microwave modeling configurations are shown to be the CMEM models 10, 6, 2. They all correspond to the Kirdyashev opacity model with Wang and Schmugge, Mironov and Dobson dielectric models, respectively. In term of SDV, most the LSMs gets best performances using the Kirdyashev model. But the best dielectric model changes depending on the LSM. Figures 9 and 10 clearly show that for any LSM, Dobson dielectric model leads to simulate larger amplitude of the signal than the Mironov or the Wang and Schmugge models. For JULES and ISBA-DF which underestimate the SDV, the use of the Dobson model improves the representation of the simulated SDV (Figure 9b and 10b). On the contrary, ISBA-FR, HTESSEL, Noah and ORCHIDEE-CWRR perform better in terms of SDV using Wang and Schmugge or Mironov than Dobson (Figure 10c,d). TESSEL and CTESSEL overestimate the simulated amplitude. For these two LSMs the best SDV and E is obtained with the Wegmüller and Wigneron models with Mironov (configurations 7 and

Table 5: Best microwave emission modeling configuration, as indexed in Table 1, for each ALMIP-MEM LSM and for each statistical index. For SDV, best microwave emission model is chosen among those presenting a correlation value larger than 0.5. For TESSEL and CTESSEL two models provide best agreement with the observation in term of correlation.

LSM	R	E	SDV
ISBA-FR	10	10	6
ISBA-DF	10	10	2
HTESEL	10	10	10
TESSEL	6/10	8	7/8
CTESSEL	6/10	8	7/8
JULES	10	10	2
Noah	10	10	6
ORCHIDEE	6	6	6

8) but the Kirdyashev model with Mironov and Wang and Schmugge models (configurations 6, 10) optimize R.

In terms of correlation, the microwave emission modeling configuration 10 provides best agreement with the AMSR-E data for almost all the LSMs. The only exception is ORCHIDEE-CWRR for which the configuration 6 provides slightly better results with the Mironov dielectric model than with the Wang and Schmugge model.

When considering the root mean square errors, best results are also obtained with the Kirdyashev vegetation opacity model for all the LSMs but TESSEL and CTESSEL. Good performances are shown by both the Wang and Schmugge and the Mironov dielectric models.

The robustness of the Kirdyashev model to provide simulated brightness temperatures in best agreement with the satellite observations is particularly noteworthy. For most LSMs considered, with corresponding errors on soil moisture and soil temperature patterns, it simulates the brightness temperatures dynamics with lowest errors and higher correlation. This robustness shown for EXP2 is also found for EXP1 (not shown), indicating a robustness to the precipitation forcing as well.

4 Summary and conclusion

ALMIP-MEM consist in a set of simulations of C-band brightness temperatures over West Africa for a one year annual cycle in 2006. Simulations have been performed for an incidence angle of 55° and results are evaluated against AMSR-E C-band data. The study encompasses 96 simulations, for 8 LSMs coupled to the Community Microwave Emission Model in 12 configurations. Each configuration corresponds to a different combination of the vegetation opacity and the soil dielectric models. Simulations are performed for the two ALMIP experiments for which different precipitation and radiative fluxes forcing are used.

The results show the critical importance of the Land Surface Models precipitation forcing for the quality of simulated brightness temperatures. Using corrected precipitation and radiative fluxes forcing leads to a much better agreement with AMSR-E observations than using forecast fluxes. The best CMEM configuration is the one that uses the Kirdyashev opacity model and the Wang and Schmugge dielectric model. The spatio-temporal correlation between simulated and observed TB, averaged among the 8 LSMs is 0.54 in EXP1 and 0.67 in EXP2. This validates the satellite based correction of precipitation forcing used in ALMIP. Conversely, this also points out the great potential offered by low frequency passive microwave remote sensing to corrected LSM errors due to precipitation forecast. Time dynamics of simulated brightness temperature is well reproduced in our simulations by the different LSMs. There is a general better agreement, in terms of dynamics, over

Sahel than over southern latitudes where the temporal correlation with observations is lower. When comparing model performances over the Agoufou super site grid-point, the different LSMs perform well in time dynamics, which is mainly controlled by the precipitation forcing. But the different LSMs perform differently in terms of absolute value and in terms of amplitude of the simulated soil moisture. LSMs errors in simulated soil moisture impact on simulated brightness temperature. Consistence in simulated soil moisture and brightness temperature evaluation against two independent data sets obtained from the Agoufou super site ground measurements and from AMSR-E space measurements, provides here a robust validation of the forward microwave emission modeling approach.

At seasonal scale, it is shown that the time-latitude pattern is very well reproduced by all the LSMs coupled to CMEM (configuration 10), with a good agreement with AMSR-E data. A wet patch characterized by lower values of brightness temperatures at horizontal polarization is observed and simulated over Sahel in August which is the period of maximum activity of the monsoon season.

ALMIP-MEM provides the first inter-comparison of microwave emission models at regional scale. Combined with the ALMIP LSM intercomparison, the study quantifies the relative importance of Land Surface Modeling and radiative transfer modeling in the monitoring of low frequency passive microwave emission on land surfaces. The scatter obtained between LSMs, concerning their performances for simulating TB, shows that land surface processes modeling impacts on the simulated brightness temperature. LSMs which take into account a fine vertical discretization in the soil do an overall better job than those which use a coarser resolution to reproduce the AMSR-E brightness temperatures. A large sensitivity in simulated TOA brightness temperature is shown to be due to the choice of the forward modeling approach. Statistical results show the suitability and the robustness of the Kirdyashev opacity model which, when used here with the ECOCLIMAP vegetation data base, provides best results for most LSMs considered in this study. For all LSMs, the combination of the Kirdyashev model with the Wang and Schmugge dielectric model leads to best performances in simulated TB in terms of correlation. The use of the Mironov model for dielectric constant provides results close to those obtained with the Wang and Schmugge model, with however higher amplitude of variations in simulated TB (higher SDV). The vegetation opacity model is the largest factor affecting the skill, in terms of correlation with AMSR-E data, of the coupled LSM-CMEM to simulate TOA TB. The dielectric model in contrast, has a higher impact than the dielectric model on the SDV of simulated TB.

In the framework of the preparation of the future SMOS satellite, the large sensitivity of simulated TOA TB to the choice of the microwave emission model, as well as the consistence of the results obtained for different LSMs, point out the importance of the forward modeling approach for soil moisture retrieval and assimilation of passive microwave data.

Acknowledgements

This work has been supported by the ECMWF and the European Space Agency (ESA) under the contract 20244/07/I-LG for the preparation of the Soil Moisture and Ocean Salinity (SMOS) mission project. The authors thank the NASA National Snow and Ice Data Center (NSIDC) for providing AMSR-E brightness temperature data. The AMMA (African Monsoon Multidisciplinary Analysis) Land Surface Model Intercomparison Project has been conducted in the framework of AMMA. Based on a French initiative AMMA was built by an international scientific group and is currently funded by a large number of agencies, especially from France, UK, US and Africa. It has been the beneficiary of major financial contribution from the European Community's Sixth Framework Research Programme. Detailed information in scientific coordination and funding is available on the AMMA International web site <http://www.amma-international.org>. The authors thank Erik Andersson for his helpful comment on the manuscript.

References

- Balsamo, G., P. Viterbo, A. Beljaars, B. van den Hurk, M. Hirsch, A. Betts, and K. Scipal (2008). A revised hydrology for the ECMWF model: Verification from field site to terrestrial water storage and impact in the Integrated Forecast System. *J. Hydrometeo.*
- Blyth, E., M. Best, P. Cox, R. Essery, O. Boucher, R. Harding, P. C., P. Vidale, and I. Woodward (2006). JULES: a new community land surface model. *IGBP Newsletter, October*.
- Boone, A. and P. de Rosnay (2007a). AMMA forcing data for a better understanding of the West African monsoon surface-atmosphere interactions. Quantification and Reduction of Predictive Uncertainty for Sustainable Water Resource Management. *IAHS Publ. 303*.
- Boone, A. and P. de Rosnay (2007b). Toward the improved understanding of land-surface processes and coupling with the atmosphere over West Africa. *LEAPS Newsletter 3*.
- Boone, A., V. Masson, T. Meyers, and J. Noilhan (2000). The Influence of the Inclusion of Soil Freezing on Simulations by a SoilVegetationAtmosphere Transfer Scheme. *J. Appl. Meteorol. 39(9)*.
- Boone, A. Habets, F., J. Noilhan, D. Clark, P. Dirmeyer, S. Fox, Y. Gusev, I. Haddeland, R. Koster, D. Lohmann, S. Mahanama, K. Mitchell, O. Nasonova, G.-Y. Niu, A. Pitman, J. Polcher, A. Shmakin, K. Tanaka, B. van den Hurk, S. V erant, D. Verseghy, P. Viterbo, and Z.-L. Yang (2004). The Rhone-Aggregation Land Surface Scheme Intercomparison Project: An Overview. *J. Climate. 17*.
- Calvet, J.-C., A.-L. Gibelin, J.-L. Roujean, E. Martin, P. Le Moigne, H. Douville, and J. Noilhan (2008). Past and future scenarios of the effect of carbon dioxide on plant growth and transpiration for three vegetation types of southwestern France. *Atmos. Chem. Phys. 8*, 397–406.
- Calvet, J.-C., J. Noilhan, J.-L. Roujean, P. Bessemoulin, M. Cabelguenne, A. Olioso, and J.-P. Wigneron (1998). An interactive vegetation SVAT model tested against data from six contrasting sites. *iAgric. For. Meteor. 37*, 73–95.
- Cardona, M., M. Vall-llossera, S. Blanch, A. Camps, A. Monerris, I. Corbella, F. Torres, and N. Duffo (2005). Properties of different soil types collected during the mouse 2004 field experiment. *IGARSS 2004, Seoul, Korea*.
- Chen, F. and J. Dudhia (2001). Coupling an advanced land surface-hydrology model with the Pen State-NCAR MM5 modeling system. Part I: Model implementation and sensitivity. *Mon. Wea. Rev 129*.
- Chopin, F., J. Berges, M. Desbois, I. Jobard, and T. Lebel (2004). Multi-scale precipitation retrieval and validation in african monsoon systems. *2nd International TRMM Science Conference, 6-10 Spet. Nara, Japan*.
- Choudhury, B., T. Schmugge, A. Chang, and R. Newton (1979). Effect of surface roughness on the microwave emission from soils. *J. Geophys. Res., 5699–5706*.
- Choudhury, B., T. Schmugge, and T. Mo (1982). A parameterization of effective soil temperature for microwave emission. *J. Geophys. Res., 1301–1304*.
- Ciais, P., M. Reichstein, N. Viovy, A. Granier, J. Ogee, V. Allard, M. Aubinet, N. Buchmann, C. Bernhofer, A. Carrara, F. Chevallier, N. De Noblet, A. Friend, P. Friedlingstein, T. Grunwald, B. Heinesch, P. Keronen, A. Knohl, G. Krinner, D. Loustau, G. Manca, G. Matteucci, F. Miglietta, J. Ourcival, D. Papale, K. Pilegaard, S. Rambal, G. Seufert, J. Soussana, M. Sanz, E. Schulze, T. Vesala, and R. Valentini (2005). Europe-wide

- reduction in primary productivity caused by the heat and drought in 2003. *Nature*, 0028–0836, 4377058, 529–533, ISI:000232004800045.
- de Rosnay, P., A. Boone, A. Beljaars, and J. Polcher (2006). AMMA Land Surface Modelling and Intercomparison Projects. *GEWEX-news. Global Energy and Water Cycle Experiment 15(1)*.
- de Rosnay, P., J.-C. Calvet, Y. H. Kerr, J.-P. Wigneron, F. Lemaître, M.-J. Escorihuela, J. Muñoz Sabater, K. Saleh, J. Barrié, G. Bouhours, L. Coret, G. Chereil, G. Dedieu, R. Durbe, N. Fritz, F. Froissard, J. Hoedjes, A. Kruszewski, F. Lavenu, D. Suquia, and P. Waldteufel (2006). SMOSREX: A long term field campaign experiment for soil moisture and land surface processes remote sensing. *Remote sens. environ. 102*, pp 377–389; doi:10.1016/j.rse.2006.02.021.
- de Rosnay, P., C. Gruhier, F. Timouk, F. Baup, E. Mougin, P. Hiernaux, L. Kergoat, and V. Le Dantec (2008). Multi-scale soil moisture measurements over the Gourma meso-scale site in Mali. *J. Hydrol.*
- de Rosnay, P., Y. Kerr, J.-P. Wigneron, J.-C. Calvet, T. Pellarin, J. Polcher, and T. Lebel (2005). Multiscale validation of SMOS brightness temperature and products over West Africa. *SMOS cal-val ESA ID 3257*, Available on <http://www.cesbio.ups-tlse.fr/us/indexsmos.html>.
- de Rosnay, P., J. Polcher, M. Bruen, and K. Laval (2002). Impact of a physically based soil water flow and soil-plant interaction representation for modeling large scale land surface processes. *J. Geophys. Res. 107 no 11*.
- Decharme, B. (2007). Influence of the runoff representation on continental hydrology using the noah and the isba land surface models. *J. Geophys. Res. 112*, D19108, doi:10.1029/2007JD008463.
- Dirmeyer, P. A., A. Dolman, and N. Sato (1999). The Pilot phase of the Global Soil Wetness Project. *Bull. Americ. Met. Soc. 80(5)*, 851–878.
- Dirmeyer, P. A., X. Gao, Z. Guo, T. Oki, and N. Hanasaki (2006). The Second Global Soil Wetness Project (GSWP-2): Multi-model analysis and implications for our perception of the land surface. *Bull. Americ. Met. Soc. 87(10)*, 1381–1397.
- d’Orgeval, T. (2006). *Impact du changement climatique sur le cycle de l’eau en Afrique de l’Ouest: Modélisation et incertitudes*. Thèse de doctorat, Université Pierre et Marie Curie, Paris VI, 16pp.
- Drusch, M., T. Holmes, P. de Rosnay, and G. Balsamo (2008). Comparing ERA-40 based L-band brightness temperatures with Skylab observations: A calibration / validation study using the Community Microwave Emission Model. *J. Hydrometeo under revision*.
- Drusch, M., E. Wood, and T. Jackson (2001). Vegetative and atmospheric corrections for soil moisture retrieval from passive microwave remote sensing data: Results from the Southern Great Plains Hydrology Experiment 1997. *J. Hydrometeo 2*, 181–192.
- Entekhabi, D., G. R. Asrar, K. J. Betts, A. K. Beven, R. L. Bras, C. J. Duffy, T. Dunne, R. D. Koster, D. P. Lettenmaier, M. L. D. B., W. J. Shuttleworth, M. T. van Genuchten, M.-Y. Wei, and E. F. Wood (1999). An agenda for land surface hydrology research and a call for the second international hydrological decade. *Bull. Am. Meteorol. Soc. 10*, 2043–2058.
- Essery, R. L. H., M. Best, R. Betts, P. Cox, and T. C.M. (2003). Explicit Representation of Subgrid Heterogeneity in a GCM Land Surface Scheme. *Journal of Hydrometeorology 4(3)*.

- Foley, J., I. Prentice, N. Ramankutty, S. Levis, D. Pollard, S. Sitch, and A. Haxeltine (1996). An integrated biosphere model of land surface processes, terrestrial carbon balance and vegetation dynamics. *Glob. Biogeochem. Cycl.* 10.
- Gao, X., P. Dirmeyer, Z. Guo, M. Zhao, B. Decharme, G. Niu, and S. Mahanama (2004). An Approach for remote sensing validation of land surface scheme on a global scale. *COLA technical report- 173*. Available from the Center for Ocean-Land-Atmosphere studies, 4041 powder Mill Rd, suite 302 Calverton, MD 20705, USA, 42pp.
- Geiger, B., C. Meurey, D. Lajas, L. Franchistéguy, D. Carrer, and J.-L. Roujean (2008). Near real-time provision of downwelling shortwave radiation estimates derived from satellite observations. *Meteorological Applications in press*.
- Gruhler, C., P. de Rosnay, Y. Kerr, E. Mougin, E. Ceschia, C. J.-C., and P. Richaume (2008). Evaluation of AMSR-E Soil Moisture Products Based on Ground Soil Moisture Network Measurements. *Geophys. Res. Letters* 35, L10405, doi:10.1029/2008GL033330.
- Hall, F., B. Meeson, S. Los, and E. Brown de Colstoun (2001). ISLSCP II: New 10+ year multi-parameter near-surface global data set including greater carbon and vegetation data. *GEWEX News, Vol. 11, No. 2, International Gewex Project Office, Silver Spring, MD, 1213*.
- Henderson-Sellers, A., A. Pitman, P. Love, P. Irannejad, and T. Chen (1995). The project for inter-comparison of land-surface parametrization schemes (PILPS): Phase 2 and 3. *Bull. Amer. Meteor. Soc.* 76, 489–503.
- Holmes, T., M. Drusch, J.-P. Wigneron, and R. de Jeu (2008). A global simulation of microwave emission: Error structures based on output from ECMWFs operational Integrated Forecast System. *IEEE Trans. Geosc. Remote Sens.* 46(3), *IEEE Trans. Geosc. and Rem. Sens.*
- Jackson, T. and O. Neill (1990). Attenuation of soil microwave emission by corn and soybeans at 1.4 and 5 GHz. *IEEE Trans. Geosc. Remote Sens.* 28(5), 978–980.
- Jackson, T. and T. Schmugge (1991). Vegetation effects on the microwave emission of soils. *Remote sens. environ.* 36, 203–212.
- Jackson, T. J., D. M. Le Vine, A. Hsu, A. Oldack, P. Starks, C. Swift, J. Isham, and M. Haken (1999). Soil moisture Mapping at regional scales using microwave radiometry: The southern great plains hydrology experiment. *IEEE Trans. Geosc. Remote Sens.* 37, 2136–2149.
- Janicot, S., A. Ali, A. Asencio, G. Berry, O. Bock, B. Bourles, G. Ganiaux, F. Chauvin, A. Deme, L. Kergoat, J.-P. Lafore, C. Lavaysse, T. Lebel, B. Marticorena, F. Mounier, J.-L. Redelsperger, C. Reeves, R. Roca, P. de Rosnay, B. Sultan, C. Thorncroft, M. Tomasini, and A. forecasters team (2007). Large scale overview of the summer monsoon over West and Central Africa during AMMA field experiment in 2006. *Ann. Geophys. under revision*.
- Jarlan, L., G. Balsamo, S. Lafont, A. Beljaars, J.-C. Calvet, and E. Mougin (2007). Analysis of Leaf Area Index in the ECMWF land surface scheme and impact on latent heat and carbon fluxes: Applications to West Africa. Technical report, ECMWF.
- Jones, A., T. Vukićević, and T. Vonder Haar (2004). A microwave satellite observational operator for variational data assimilation of soil moisture. *J. Hydrometeorol* 5, 213–229.
- Kerr, Y. H. and E. G. Njoku (1990). A semi empirical model for interpreting microwave emission from semiarid surfaces as seen from space. *IEEE Trans. Geosc. Remote Sens.* 28, 384–393.

- Kerr, Y. H., P. Waldteufel, J.-P. Wigneron, J.-M. Martinuzzi, J. Font, and M. Berger (2001). Soil moisture retrieval from space: The soil moisture and ocean salinity (smos) mission. *IEEE Trans. Geosc. Remote Sens.* 39 (8), 1729–1735.
- Kirdyashev, K., A. Chukhlantsev, and A. Shutko (1979). Microwave radiation of the earths surface in the presence of vegetation cover. *Radiotekhnika i Elektronika* 24, 256–264.
- Koster, R. D., P. Dirmeyer, Z. Guo, G. Bonan, P. Cox, C. Gordon, S. Kanae, E. Kowalczyk, D. Lawrence, P. Liu, C. Lu, S. Malyshev, B. McAvaney, K. Mitchell, D. Mocko, T. Oki, K. Oleson, A. Pitman, Y. Sud, C. Taylor, D. Verseghy, R. Vasic, Y. Xue, and T. Yamada (2004). Regions of strong coupling between soil moisture and precipitation. *Sciences* 305.
- Krinner, G., N. Viovy, N. de Noblet-Ducoudré, J. Ogée, J. Polcher, P. Friedlingstein, P. Ciais, S. Sitch, and I. Prentice (2005). A dynamic global vegetation model for studies of the coupled atmosphere-biosphere system. *Global Biogeochem. Cycles* 19, GB1015, doi:10.1029/2003GB002199.
- Lebel, T., D. Parker, B. Bourles, C. Flamant, B. Marticorena, C. Peugeot, A. Gaye, J. Haywood, E. Mougin, J. Polcher, J.-L. Redelsperger, and C. D. Thorncroft (2006). The AMMA field campaigns: Multiscale and multidisciplinary observations in the West African region. Submitted to Bulletin of the American Meteorological Society. *Bulletin of the American Meteorological Society* 88(3).
- Lettenmaier, D. (2003). PILPS Special issue - Preface. *Global and Planetary change.* 38, vii–ix.
- Masson, V., J.-L. Champeaux, F. Chauvin, C. Meriguet, and R. Lacaze (2003). A global database of land surface parameters at 1-km resolution in meteorological and climate models. *J. Climate.* 97(1r61), 1261–1282.
- Milly, P. C. D. and K. A. Dunne (1994, April). Sensitivity of the global water cycle to the water-holding capacity of land. *J. Climate.* 7, 506–526.
- Mironov, V., M. Dobson, V. Kaupp, S. Komarov, and V. Kleshchenko (2004). Generalized refractive Mixing dielectric model for moist soils. *IEEE Trans. Geosc. Remote Sens.* 42(4), 773–785.
- Nepstad, D. C., C. R. Carvalho, E. A. Davidson, P. H. Jipp, P. A. Lefebvre, G. H. Negrelros, E. D. da Silva, S. E. Stone, T. A. and Trumbore, and S. Vieira (1994, December). The role of deep roots in the hydrological and carbon cycles of amazonian forests and pastures. *Nature* 372, 666–669.
- Njoku, E. G. (2004). updated daily. AMSR-E/AQUA daily L3 surface soil moisture, interpretive parms, & QC EASE-Grids. Boulder, CO, USA: National Snow and Ice Data Center Digital Media.
- Njoku, E. G., T. Jackson, V. Lakshmi, T. Chan, and S. Nghiem (2003). Soil moisture retrieval from AMSR-E. *IEEE Trans. Geosc. Remote Sens.* 41(2), 215–229.
- Noilhan, J. and S. Planton (1989). A simple parameterization of land surface fluxes processes for meteorological models. *Mon. Weather. Rev.* 117, 536–549.
- Pellarin, T., H. Kerr, and J.-P. Wigneron (2006). Global Simulation of Brightness Temperatures at 6.6 and 10.7 GHz Over Land Based on SMMR Data Set Analysis. *IEEE Trans. Geosc. Remote Sens.* 44(9), 2492–2505.
- Pellarin, T., J.-P. Wigneron, J.-C. Calvet, M. Berger, H. Douville, P. Ferrazzoli, Y. H. Kerr, E. Lopez-Baeza, J. Pulliainen, L. Simmonds, and P. Waldteufel (2003). Two-year global simulation of L-band brightness temperature over land. *IEEE Trans. Geosc. Remote Sens.* 41(4), 2135–2139.

- Redelsperger, J.-L., C. Thorncroft, A. Diedhiou, T. Lebel, D. Parker, and J. Polcher (2006). African Monsoon, Multidisciplinary Analysis (AMMA): An International Research Project and Field Campaign. *Bull. Amer. Meteorol. Soc* 87(12), 1739–1746.
- Schmugge, T. (1992). A dielectric model of the vegetation effects on the microwave emission from soils. *IEEE Trans. Geosc. Remote Sens.* 30, 757–760.
- Taylor, C. (2008). Intraseasonal land-atmosphere coupling in the west african monsoon. *J. Climate*. *accepted*.
- Taylor, C., D. Parker, and P. Harris (2007). An observational case study of mesoscale atmospheric circulations induced by soil moisture. *Geophys. Res. Letters* 34, doi:10.1029/2007GL030572.
- Taylor, K. (2001). Summarizing multiple aspects of model performance in a single diagram. *J. Geophys. Res.* 106, 7183–7192.
- Viterbo, P. and A. C. M. Beljaars (1995, March). An improved land surface parameterization scheme in the ecmwf model and its validation. Technical report, ECMWF.
- Wang, J. R. and T. Schmugge (1980). An empirical model for the complex dielectric permittivity of soils as a function of water content. *IEEE Trans. Geosc. Remote Sens.* 18, 288–295.
- Wegmüller, U., C. Mätzler, and E. Njoku (1995). Canopy opacity models, in passive microwave remote sensing of land-atmosphere interactions. *B. et al. Ed. Utrecht, The Netherlands: VSP*, 375.
- Wigneron, J.-P., J.-C. Calvet, and Y. H. Kerr (1996). Monitoring water interception by crop fields from passive microwave observations. *Agric. For. Meteorol.* 80, 177–194.
- Wigneron, J.-P., A. Chanzy, J.-C. Calvet, and N. Bruguier (1995). A simple algorithm to retrieve soil moisture and vegetation biomass using passive microwave measurements over crop fields. *Remote sens. environ.* 51, 331–341.
- Wigneron, J.-P., Y. H. Kerr, P. Waldteufel, K. Saleh, M.-J. Escorihuela, P. Richaume, P. Ferrazzoli, P. de Rosnay, R. Gurney, J.-C. Calvet, M. Guglielmetti, B. Hornbuckle, C. Mtzler, T. Pellarin, and M. Schwank (2007). L-band Microwave Emission of the Biosphere (L-MEB) Model: description and calibration against experimental data sets over crop fields. *Remote sens. environ.* 107, 639–655.